



Aeroelastic Real-Time Hybrid Simulation. I: Validation

Jie Dong, Ph.D., Aff.M.ASCE¹; Steven F. Wojtkiewicz, Ph.D., M.ASCE²; Sergio Lobo-Aguilar, Ph.D.³; Yuan Yuan, Ph.D.⁴; and Richard E. Christenson, Ph.D., M.ASCE⁵

Abstract: An innovative experimental method, called aeroelastic real-time hybrid simulation (aeroRTHS), is proposed to study the aero-dynamic vibrations of a building model in a boundary layer wind tunnel (BLWT). The aeroRTHS method aims to capture the dynamic interactions between an aeroelastic structure and the applied wind load to accurately characterize complicated, unstable phenomena such as vortex-induced vibration, and in doing so, to broaden the application of real-time hybrid simulation (RTHS) from seismic applications to wind engineering. The aeroRTHS tests were conducted in the BLWT at the University of Florida Natural Hazards Engineering Research Infrastructure Equipment Facility (UF NHERI EF). A 1-m-tall rigid physical model with an aspect ratio (height/width) of 7.3 was mounted on a modified single-axis shake table converting translational motions to corresponding rotations at the base of the model allowing the model to behave in the wind tunnel as an aeroelastic structure. A total of 128 pressure sensors located on the cross-wind sides of the physical building model measured wind pressures which then were converted to equivalent forces and ultimately resolved into a single equivalent force at the top of the physical building model based on the moment equilibrium at its base. The results from a series of aeroRTHS tests in the BLWT are reported herein to constitute a proof-of-concept study that validates the aeroRTHS method and demonstrates the aeroelastic effects on a flexible and slender structure. **DOI: 10.1061/JENMDT.EMENG-7158.** © 2024 American Society of Civil Engineers.

Introduction

Due to large aspect ratios and flexible characteristics, many modern structures are vulnerable to wind excitation; various studies have observed that tall buildings can be sensitive to wind loading in the cross-wind direction (Gu and Quan 2004; Lin et al. 2005). Vortex-induced vibration (VIV) is a wind-induced oscillation in the cross-wind direction, most commonly occurring in high-rise buildings with a large aspect ratio (Holmes 2018). This phenomenon can cause occupant discomfort, serviceability issues, fatigue (e.g., in marine risers), or even structural collapse (e.g., the Tacoma Narrows Bridge). Thus, it is critical for engineers to fully understand the behavior and condition of structures undergoing this type of wind-induced vibration.

There are three primary types of methods to evaluate structural performance under wind loading: full-scale field measurements of wind effects; numerical modeling employing computational fluid dynamics (CFD) or CFD coupled with the finite-element method (FEM); and wind tunnel experimental tests.

Full-scale field measurements of wind effects have been conducted around the world and can capture structural responses under authentic wind conditions. For example, field measurements of

Note. This manuscript was submitted on January 8, 2023; approved on October 22, 2023; published online on June 28, 2024. Discussion period open until November 28, 2024; separate discussions must be submitted for individual papers. This paper is part of the *Journal of Engineering Mechanics*, © ASCE, ISSN 0733-9399.

wind effects for three full-scale buildings in Chicago were conducted by installing four force balance accelerometers atop each building, and the in situ results were in good agreement with those from wind tunnel tests (Li et al. 1998; Kilpatrick et al. 2003; Gu and Quan 2004; Li et al. 2007). A series of full-scale measurements of wind effects also were conducted on high-rise buildings such as the Jin Mao Tower, Di Wang Tower, and Guangzhou West Tower in China (Li et al. 1998, 2008, 2014); the Republic Plaza building in Singapore; the Lotte World Tower in South Korea; and the Burj Khalifa in the United Arab Emirates (Kijewski-Correa et al. 2012; Bashor et al. 2012; Amezquita-Sanchez et al. 2017). These field tests fully captured the aeroelastic coupling between the building and wind. However, the key parameters for the wind loading and structures are unique and localized (Melbourne 1977; Tamura et al. 1993; Li et al. 1998). Consequently, it can be challenging to conduct comprehensive studies for various meteorological conditions. Additionally, the required preparation for tests and data recording may be time- and cost-intensive (Kato et al. 1992; Li et al. 2007).

CFD has become a commonly applied tool for analyzing fluid flows around building structures. Tremendous advancements have occurred in the last several decades (Choi 1993; Reichrath and Davies 2002; Blocken and Carmeliet 2004; Stathopoulos 2006; Norton et al. 2007; Mochida and Lun 2008; Blocken et al. 2013; Blocken 2014). However, a potential limitation of CFD is that it requires modeling expertise and judgment. For example, researchers differ on the choice of the turbulence models and boundary conditions to obtain accurate results. In addition, large computational times are required if the simulated models are too complex and/or the wind phenomena are complicated.

Wind tunnel experimental tests are effective for the evaluation of wind loading on a structure. In wind tunnel testing, high-frequency base balance (HFBB) is a powerful method to measure wind-induced forces (Davenport 1967; Tschanz and Davenport 1983); it has been used extensively to characterize wind forces in terms of mean, RMS, and peak wind loads (Xie and Irwin 1998). Parameters such as side ratio, aspect ratio, and building shape have different impacts upon along-wind vibration, cross-wind vibration, and

¹Dept. of Civil and Environmental Engineering, Clarkson Univ., Potsdam, NY 13699. Email: jie.dong@clarksonalumni.com

²Professor, Dept. of Civil and Environmental Engineering, Clarkson Univ., Potsdam, NY 13699 (corresponding author). Email: swojtkie@clarkson.edu

³Assistant Professor, Civil Engineering School, Univ. of Costa Rica, San José 11501, Costa Rica. Email: sergio.lobo@ucr.ac.cr

⁴Dept. of Civil and Environmental Engineering, Univ. of Connecticut, Storrs, CT 06269. Email: yuan.2.yuan@uconn.edu

⁵Professor, Dept. of Civil and Environmental Engineering, Univ. of Connecticut, Storrs, CT 06269. Email: richard.christenson@uconn.edu

torsional response (Lin et al. 2005; Amin and Ahuja 2014). An online interactive database integrated with HFBB technique in wind tunnels was created for structural wind resistance design based on a total of 27 model buildings (Zhou et al. 2003). Two standard buildings, specified as basic and advanced building models, were proposed in the international HFBB benchmark study (Holmes and Tse 2014). Another widely used measurement method in wind tunnel testing is High Frequency Pressure Integration (HFPI) (Steckley et al. 1992). In addition, synchronous multi-pressure sensing system (SMPSS) (Chen et al. 2020; Aboutabikh et al. 2022), also known as Synchronous Pressure Acquisition Network (SPAN) (Cermak 1995), is a widely used instrumentation technique. Instead of the installation of a load cell at the base of a testing model in the wind tunnel, the HFPI technique executes multiple pressure measurements at selected locations on a model building's exterior surface. The wind-induced responses were evaluated by comparing those obtained using the standard CAARC tall building model, employing the HFBB and HFPI techniques for testing (Dragoiescu et al. 2006). The results with regard to base moments and torsions from these two methods had good agreement, and therefore both HFBB and HFPI were able to offer an accurate dynamic analysis for the rigid models under wind loading. Neither of these methods has the ability to account for the scaled model vibrating aeroelastically. Additionally, when using HFBB, forces and moments are known only at the base of the model, and the forces are assumed to vary linearly along the height of the scaled model, ignoring any spatial variations of pressure distribution (Cermak 2003).

Enhancing these various aeroelastic test methods with Real-Time Hybrid Simulation (RTHS), this paper proposes an aerodynamic Real-Time Hybrid Simulation (aeroRTHS) framework that can address the current challenges with the time and resources needed to conduct comprehensive wind tunnel studies and the expertise and computational resources needed for numerical modeling. The aeroRTHS framework can facilitate the rapid creation, investigation, and validation of the next generation of mitigation strategies by fully capturing the complex fluid-structure interaction in these systems needed to investigate the aeroelastic response from wind hazards. The implementation of this framework at the boundary layer wind tunnel at the UF NHERI EF is intended to accelerate adoption of this framework and more broadly ensure the reliability and resilience of the nation's infrastructure by enabling the investigation of an increased number of hazard mitigation approaches applied to more realistic situations in a nondestructive, cost-effective manner.

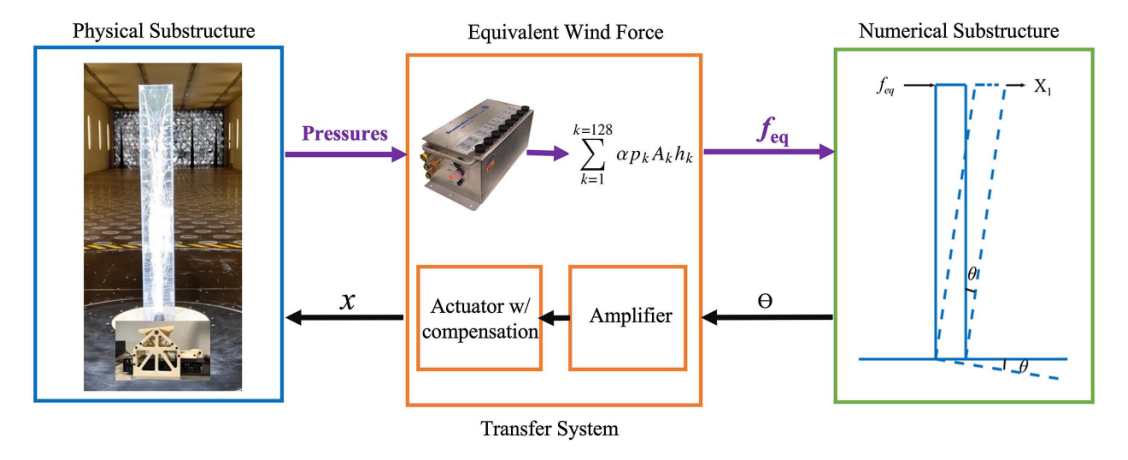


Fig. 1. Schematic of aeroRTHS at the UF Boundary Layer Wind Tunnel.

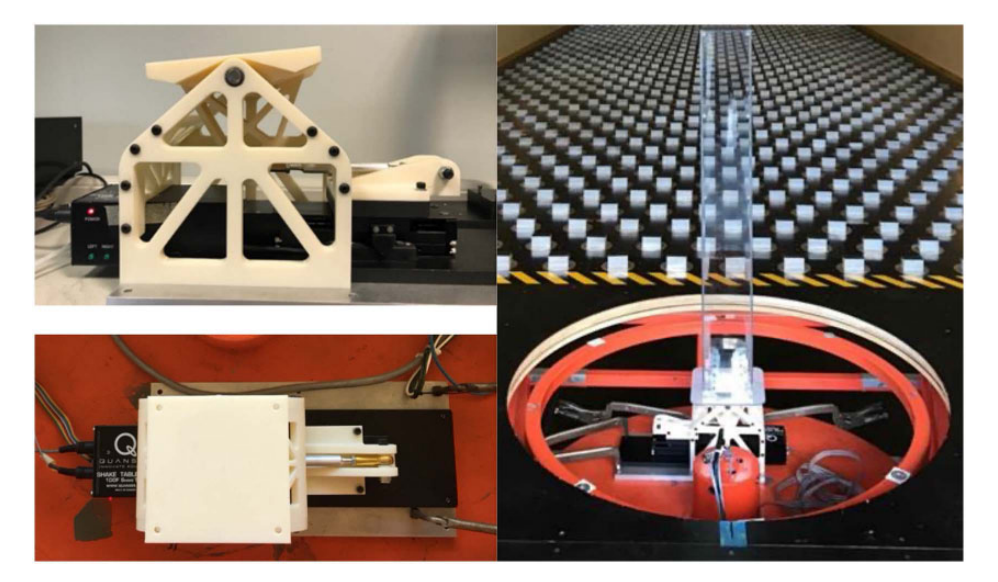


Fig. 2. aeroRTHS transfer system with 3D printed rotational platform and Quanser Shake Table I-40.

Real-Time Hybrid Simulation

Hybrid simulation or pseudo-dynamic analysis initially was proposed to study a cantilever beam under dynamic loading (Hakuno et al. 1969). Hybrid simulation combines the high fidelity of experimental tests and the utility of numerical simulations. Building on that initial work, and with advances in digital computing, hybrid simulation has been applied to study structures under seismic response (Dermitzakis and Mahin 1985; Takanashi and Nakashima 1987; Shing et al. 1996). To examine a rate-dependent specimen, real-time hybrid simulation (RTHS) was proposed to investigate the dynamic response of a structure (Darby et al. 1999; Jung and Shing 2006; Carrion 2008; Christenson et al. 2008).

The application of RTHS for aerodynamic vibration of structures was proposed by Kanda (Kanda 1995; Kawaguchi et al. 1999). The hybrid vibration system (HVS) and hybrid aerodynamic vibration technique (HAT) were used to investigate the windinduced response of elastoplastic models in wind tunnel tests (Kawaguchi et al. 2001; Kanda et al. 2003). In these approaches, wind forces were measured as in HFBB with a load cell mounted underneath the building model as a force balance device, and the base was actuated to rotate the computed displacement. The force balance device captured both the aerodynamic forces and inertial forces generated by the test model, which proved challenging to remove during the simulations. Pressure sensors distributed on the building model as in HFPI replaced the load cell to measure the external wind forces acting on the model in the modified hybrid aerodynamic vibration technique (MHAT) (Nishi and Kanda 2010; Kato and Kanda 2014). The MHAT method was able to simulate aerodynamic vibrations of structures, including unstable phenomena such as VIV and galloping of a three-dimensional square prism made of a low mass density polypropylene in a smooth flow condition.

The aeroRTHS method proposed herein is an extension of RTHS and MHAT to capture aeroelastic structural response under wind excitation. The aeroRTHS framework system is outlined and its feasibility assessed by analyzing the vortex-induced vibration for different structural models under a series of constant mean wind speeds.

AeroRTHS Framework

The concept of aeroRTHS combines the complementary advantages of both experimental wind tunnel testing and numerical modeling to investigate the aeroelastic response of flexible buildings. The major advantages are that (1) accurate wind pressure data are measured on an aeroelastic physical building model in a BLWT; and (2) the measured wind force at each time step of the simulation is used to determine the motion of the building in the BLWT using a numerical model with given dynamic parameters. Fig. 1 provides the schematic of aeroRTHS as implemented in the BLWT at the University of Florida Natural Hazards Engineering Research Infrastructure Equipment Facility (UF NHERI EF). This BLWT is an open-loop low-speed wind tunnel 6-m wide × 3-m tall × 40-m long (Catarelli et al. 2020a, b).

Experimental Substructure

The physical building specimen was a plexiglass building model with a dimensions of 13.7 cm (5.39 in.) \times 13.7 cm \times 100 cm (39.37 in.), and the mass (weight) of the building model was 4.12 kg (9.08 lb). The model had an aspect ratio of 7.3, and therefore was regarded as a wind-sensitive structure (Yang et al. 2004). The building was slender and symmetric about both horizontal directions; its elastic center was coincident with the axis of the mass

center to prevent coupled lateral-torsional responses (Holmes et al. 2003). The physical building model had 128 pressure sensors installed on its cross-wind sides.

In aeroRTHS wind tunnel testing, the numerically determined displacements at the numerical–physical boundary are enforced on the physical specimen to insure coordinate compatibility through a transfer system (Nakata et al. 2014). The transfer system was single-axis, Quanser Shake Table, Model I-40 combined with a three-dimensionally (3D) printed platform. The shake table consisted of a stage (slip table) mounted on a high-quality, low-backlash linear

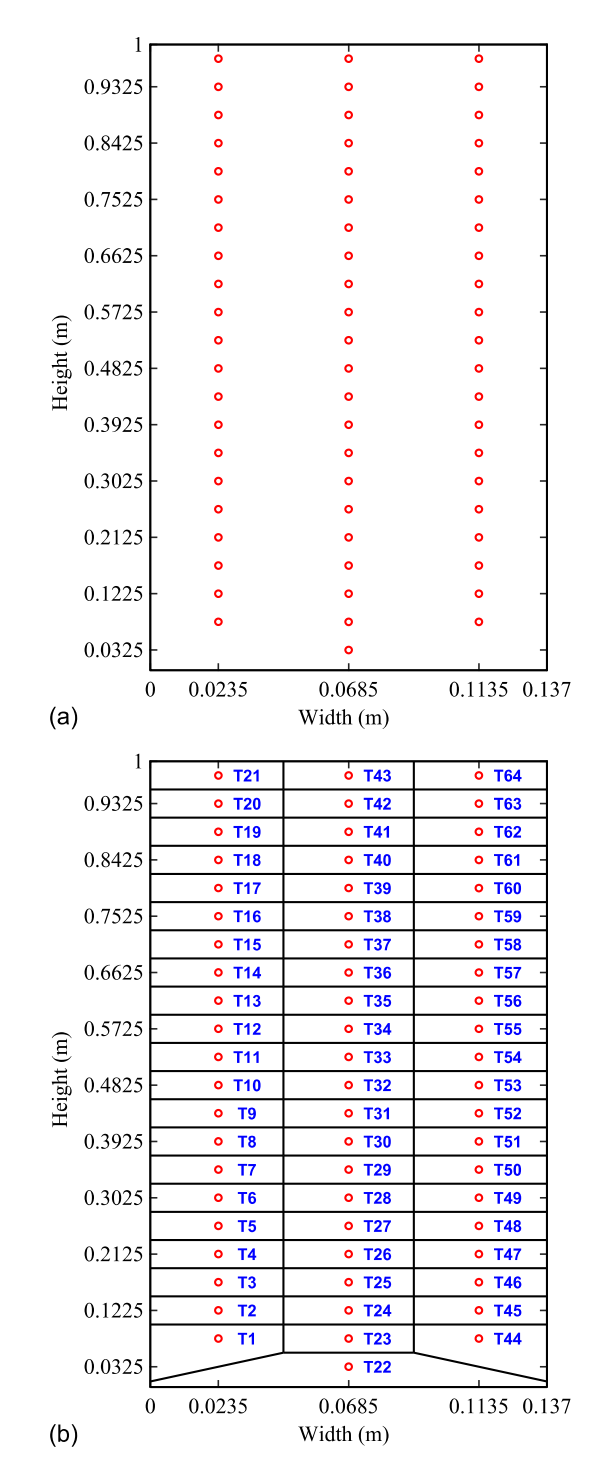


Fig. 3. Voronoi diagram and physical setup: (a) pressure sensor locations; and (b) tributary areas.

guide with a total journey of 40.00 mm, which was driven by a hightorque direct-drive DC servomotor. A high-resolution encoder enabled the system to obtain a linear stage position resolution of 1.22 μm . To provide a necessary rotational degree-of-freedom at the numerical–physical boundary used in these tests, a rotational platform was added to the top of the shake table to transform the linear motion of the stage to the rotational motion of the platform to which the base of the building model was attached. The rotational platform, which provided base rotations of $\pm 10^\circ$, was 3D printed and affixed to the Quanser (Markham, Ontario, Canada) Shake Table I-40; Fig. 2 shows the side view and top view, and the base and platform mounted in the BLWT with a building model attached. The resulting aeroRTHS transfer system satisfied the space constraints for the installation under the test floor in the UF BLWT.

Table 1. Tributary areas for all 64 pressure taps

Tap number	Area (m ²)
T1, T44	0.003128
T45-T64	0.002070
T22	0.005419
T23-T43	0.002025

A ZOC33 Scanivalve miniature pressure scanner (Liberty Lake, Washington) located on two opposite cross-wind faces of the physical model at a sampling rate of 200 Hz. To provide a consistent influence on the pneumatic frequency response of pressure instrumentation, a uniform 120 cm length of tubing was used for each pressure sensor.

Numerical Substructure

For this aeroRTHS test, a single degree-of-freedom (SDOF) linear model was chosen to numerically represent the dynamic properties of the building model as it rotated about its base.

The rotational equation of motion of the building model is given by

$$I_r \ddot{\theta}(t) + c_r \dot{\theta}(t) + k_r \theta(t) = M_r(t) \tag{1}$$

where I_r = rotational moment of inertia; c_r is the rotational damping; k_r = rotational stiffness; M_r = external moment vector; and θ , $\dot{\theta}$, and $\ddot{\theta}$ = angular displacement, velocity, and acceleration of the model, respectively.

The moment of inertia of the building model about the base is

$$I_r = \frac{1}{3}m_p h^2 \tag{2}$$

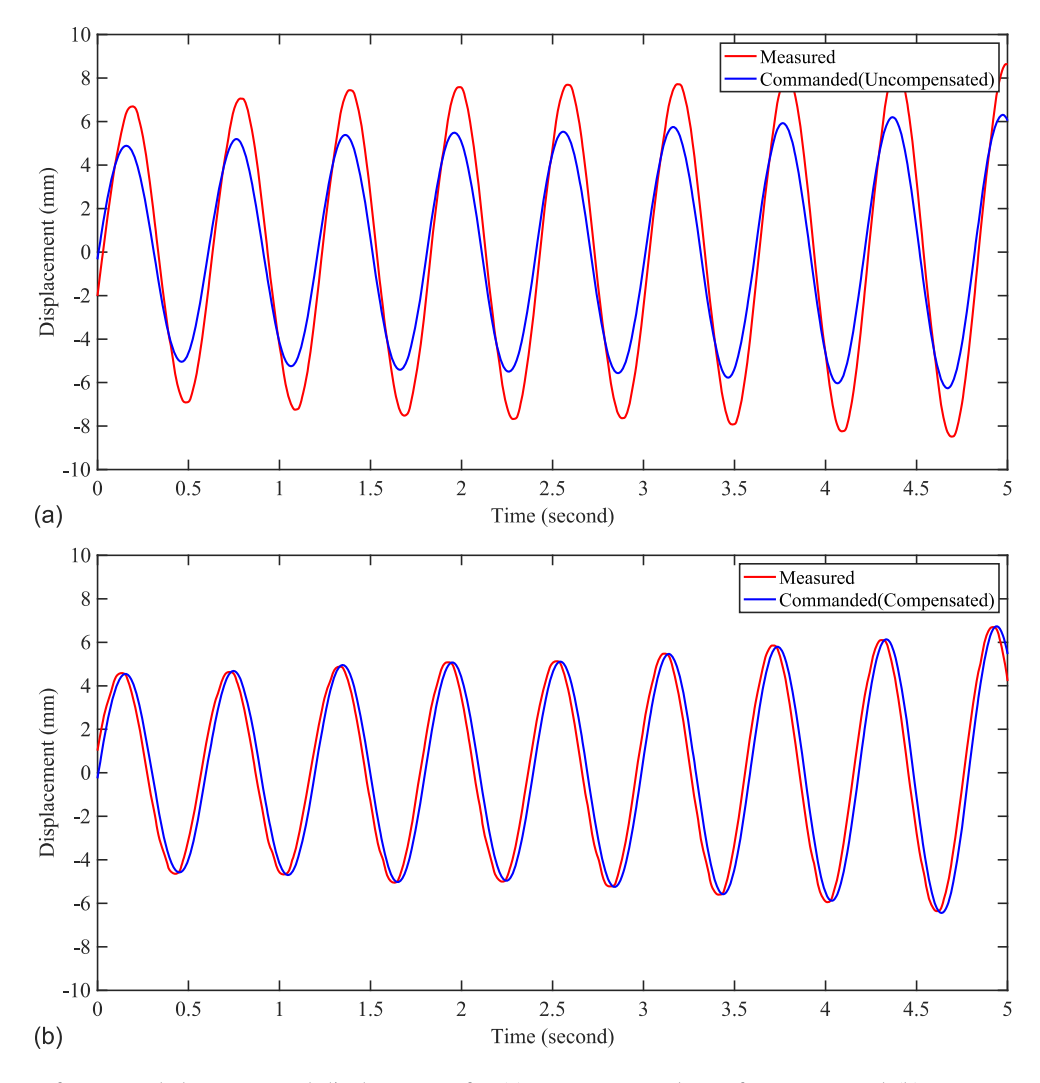


Fig. 4. Time history of commanded to measured displacements for (a) uncompensated transfer system; and (b) compensated transfer system.

where m_p = mass of physical model (4.12 kg); and h = rigid model's height.

A linear relationship exists between the rotation, θ , at the base of the building model and the translational displacement, x, on the top of the building model. A linear relationship was obtained between the moment, M_r , at the base of the physical building specimen, and a theoretical force applied at the top, f_{eq} . These are given by

$$x = h \cdot \theta \tag{3}$$

$$M_r = h \cdot f_{eq} \tag{4}$$

Substituting Eqs. (3) and (4) into Eq. (1) yields

$$\frac{m_p}{3}\ddot{x}(t) + \frac{c_r}{h^2}\dot{x}(t) + \frac{k_r}{h^2}x(t) = f_{eq}(t)$$
 (5)

Next, rewriting Eq. (5) in standard form obtains

$$\tilde{m}\ddot{x}(t) + \tilde{c}\dot{x}(t) + \tilde{k}x(t) = f_{eq}(t)$$
(6)

where $\tilde{m} = m_p/3$ for the aeroelastic flexible-base models (FMs) FM1, FM2, and FM4, and $\tilde{m} = (2/3)m_p$ for FM3; $k_r = 4\tilde{m}\pi^2h^2f_n^2$; $c_r = 4\pi\zeta f_n\tilde{m}h^2$; f_{eq} is the single equivalent force vector at the top of the building; and x, \dot{x} , and \ddot{x} = translational displacement, velocity,

and acceleration of the model at its top, respectively. The equation of motion Eq. (6) can be rewritten in terms of natural frequency, $\omega_n = \sqrt{\tilde{m}/\tilde{k}}$, and building model's damping ratio, ζ , as

$$\ddot{x}(t) + 2\zeta\omega_n\dot{x}(t) + \omega_n^2 x(t) = \frac{1}{\tilde{m}} f_{eq}(t)$$
 (7)

A Voronoi diagram was adopted to determine pressure taps' tributary areas without subjective bias (Guibas and Stolfi 1985; Aurenhammer 1991; Gierson et al. 2017).

A Voronoi diagram consists of a number of polygons created by drawing perpendicular bisectors to three lines of triangles. These triangles are created from a Delaunay triangulation that connects a given set of sites (pressure sensors, in this case) to form nonoverlapping triangles. Only one tap is allowed to be in each polygon in which any interior point is closer to this pressure tap than to any other. Thus, it is assumed that the pressure is equally distributed in one polygon, and its value is measured from the pressure tap within. Because the geometry of the model and locations of pressure taps are unchanged during all aeroRTHS tests, tributary areas for all pressure taps could be precalculated only once, avoiding unnecessarily repeated computation.

If all pressure data at a certain time are captured along with known tributary areas, a single aerodynamic force acting at the top

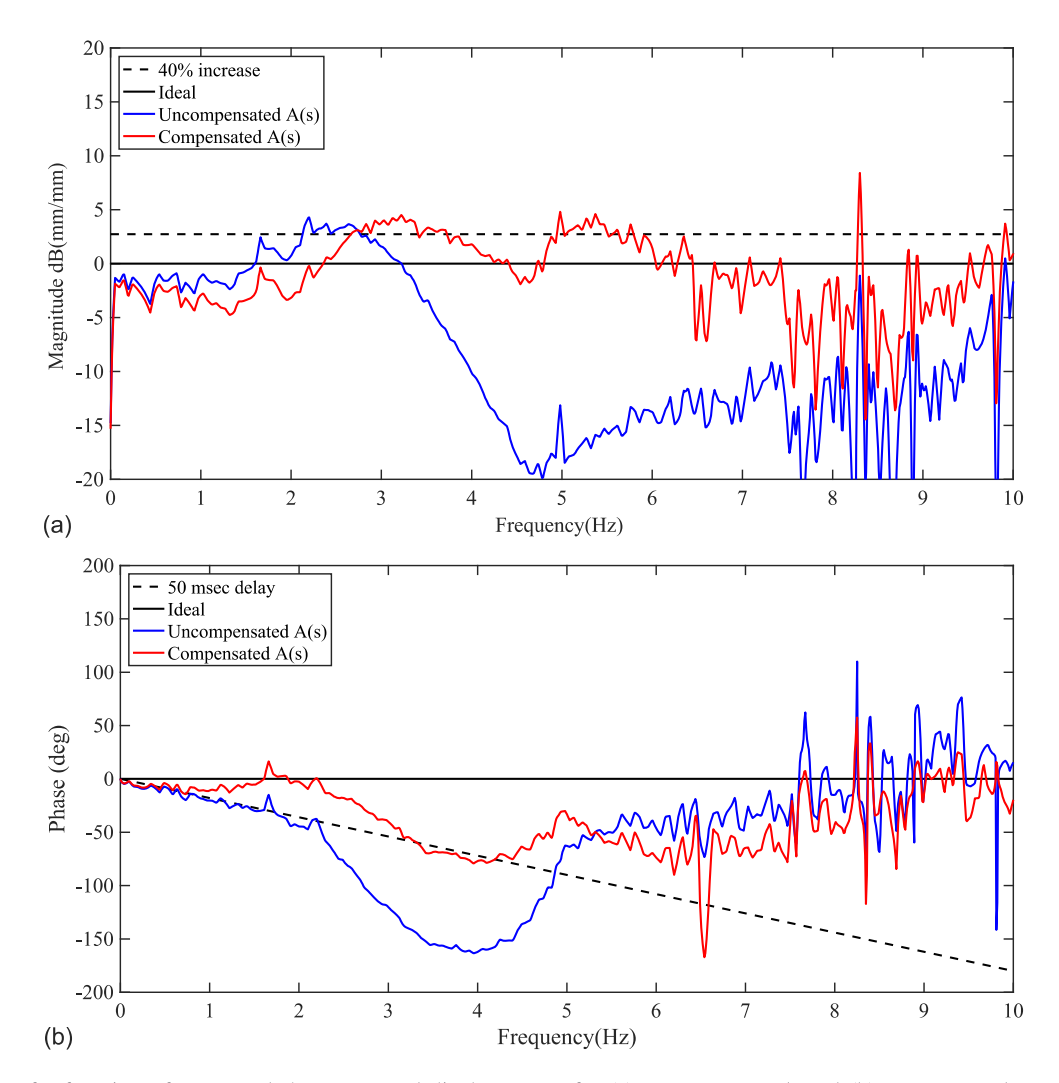


Fig. 5. Transfer function of commanded to measured displacements for (a) uncompensated; and (b) compensated transfer system.

of the experimental model can be computed as a function of the measured pressures, associated tributary areas, and the height above the base

$$f_{eq}(t) = \frac{1}{h} \sum_{k=1}^{k=128} \alpha p_k(t) A_k h_k$$
 (8)

where h = rigid model's height; $\alpha = \text{sign}$ of normal direction (± 1 , where +1 is the force normal inward to the physical building model); $p_k = \text{wind}$ pressure of kth pressure tap at time t; $A_k = k$ th tributary area of kth pressure tap; and $h_k = k$ th tap's height above ground level.

Figs. 3(a and b) show the locations of sensors and the associated tributary areas used during the aeroRTHS tests. Each row except the first row had three pressure taps embedded at uniform 4.5 cm intervals; a total of 22 rows with 64 pressure taps were included on each cross-wind face. The sizes of circles in Fig. 3 are not the actual diameters of taps; they indicate the locations of the centers of these taps. The tributary areas for all 64 pressure taps are presented in Table 1.

Compensation for Transfer System

It is essential for a stable and accurate RTHS that the transfer system provides accurate tracking in both magnitude and phase. The uncompensated transfer system was observed to have both magnitude and phase distortion. A sinusoidal input, synchronized with the building structure's fundamental natural frequency of 1.65 Hz,

was commanded to the aeroRTHS transfer system. Increasing amplitudes from approximately 5 to 7 mm, corresponding to rotations of approximately 0.29°–0.4°, were investigated. A time-history plot of the commanded and measured stage displacements is shown in Fig. 4(a). It was observed that the measured displacement, while varying at 1.65 Hz, had a magnitude approximately 40% larger, and time delays of as much as 50 ms were observed.

The transfer function of the transfer system was determined (Bendat and Piersol 2010) by commanding a band-limited white noise input with a measured displacement output. A model-based feedforward compensator was employed to improve the displacement tracking in both amplitude and phase of the transfer system. The compensator was determined by fitting the transfer function numerator and denominator polynomials to the experimentally measured transfer function, inverting the transfer function, and adding poles to ensure that the resulting compensator was stable. The resulting compensator, C(s), is given by

$$C(s) = \frac{C_1(s)}{C_2(s)} \tag{9}$$

$$C_1(s) = 50,008.9 \times (s^3 + 136.72s^2 + 1580.7s + 24010)$$

$$C_2(s) = (s^5 + 207.47s^4 + 103380s^3 + 2.0944 \cdot 10^6s^2 + 1.1172 \cdot 10^8s + 1.2735 \cdot 10^9)$$

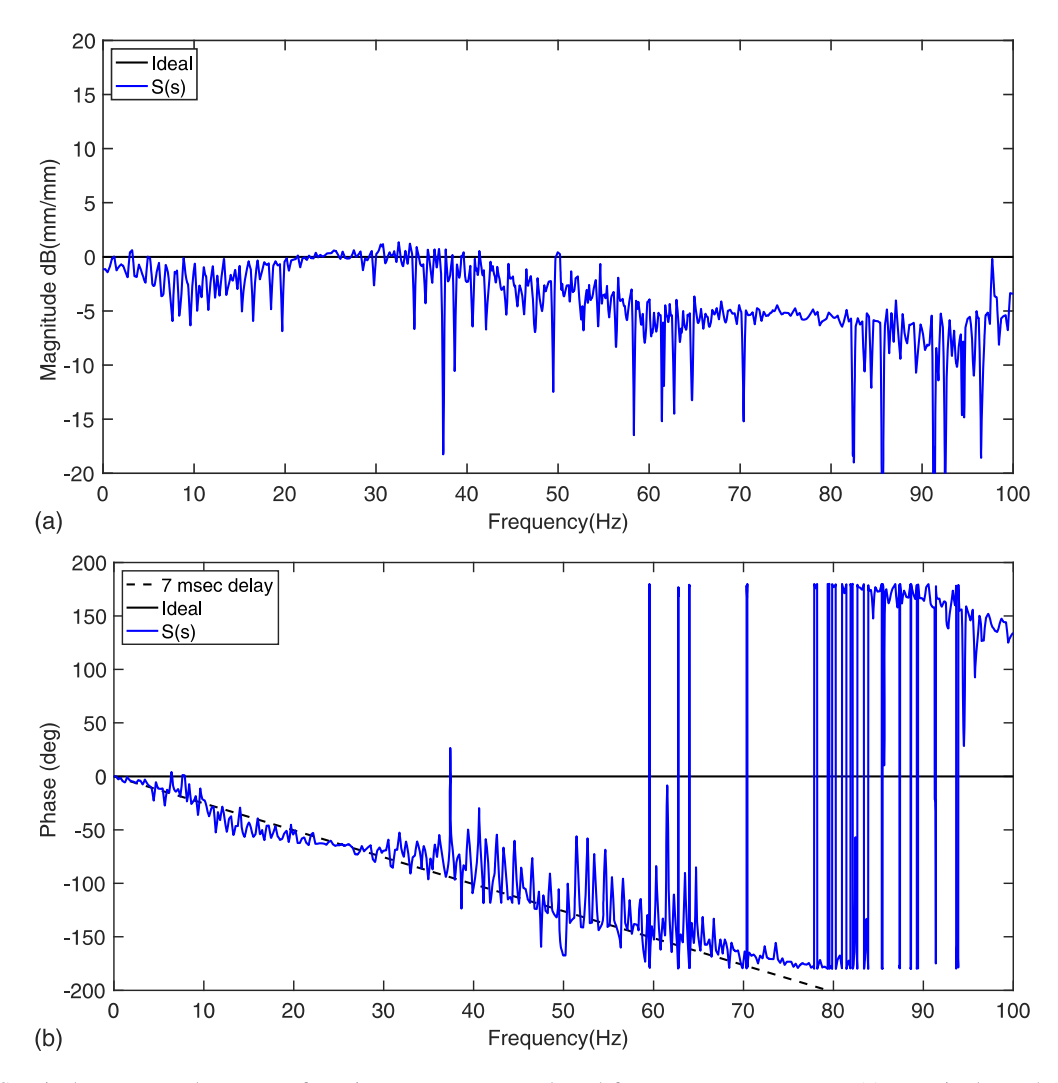


Fig. 6. Scanivalve measured response from input pressure over broad frequency range system: (a) magnitude; and (b) phase.

The time history of the compensated transfer system is shown in Fig. 4(b). The measured displacement had a magnitude within 1% of the commanded displacement and actually led the commanded displacement by approximately 20 ms. The magnitude and phase tracking were improved significantly over the bandwidth of interest (0–2.25 Hz) with the use of the model-based feedforward compensator (Fig. 5).

Compensation of Pressure Tube Measurements

Compensation related to pressure wave shift and amplitude change of the pressure equipment also was calibrated for this pressure instrumentation (Gerstoft and Hansen 1987; Pemberton 2010). A sampling rate of 200 Hz was chosen, which was fast enough to capture significant flow characteristics associated with the vortex

shedding. The measured frequency response of the Scanivalve pressure sensors has been documented to have distortion of magnitude and phase (Pemberton 2010). The transfer functions of the University of Florida Scanivalve system were determined previously for various fixed tubing lengths (Gerstoft and Hansen 1987). The uniform 120 cm length of tubing used in this study corresponded to the measured transfer function in Fig. 6. As with the transfer system, ideally the transfer function is identity, with a magnitude of 0 dB and a phase of 0°. The magnitude varied over a frequency range from 0 to 100 Hz, and the phase had an apparent time delay of 7 ms.

A model-based feedforward compensator was employed to improve the pressure tracking of the Scanivalve system in a similar fashion as for the transfer system. The resulting compensator for the Scanivalve sensor, D(s), is

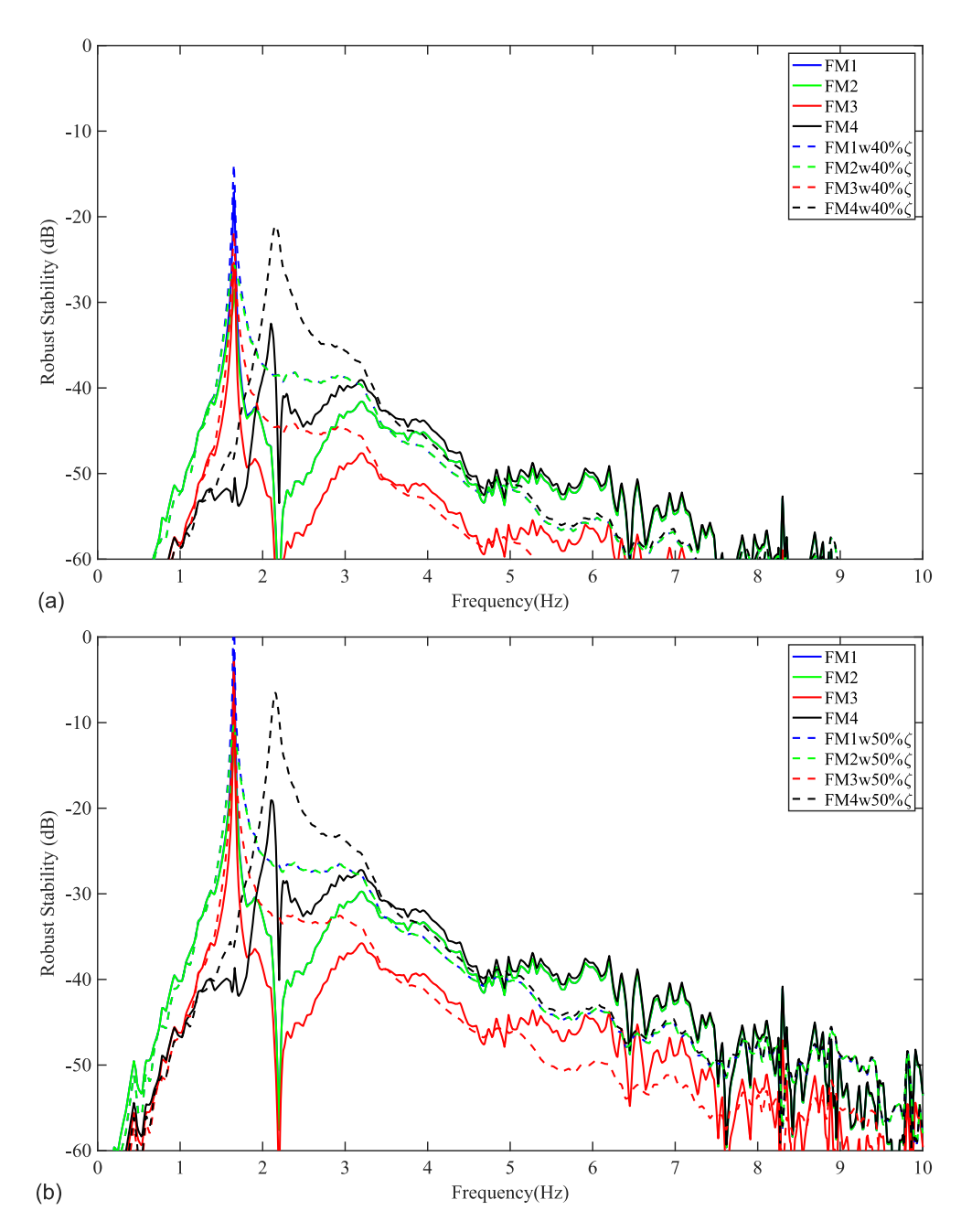


Fig. 7. Robust stability analysis over bandwidth of interest for FMs 1–4 at negative aeroelastic damping of (a) 60% of inherent damping; and (b) 50% of inherent damping.

$$D(s) = \frac{D_1(s)}{D_2(s)} \tag{10}$$

 $D_1(s) = 9.8696 \cdot 10^4 s + 9.3019 \cdot 10^6$ $D_2(s) = 84.8230 s^2 + 4.2637 \cdot 10^4 s + 8.3717 \cdot 10^6$

Robust Stability Analysis

Prior to calculating any RTHS test, it is critical to understand and predict both the stability and performance (accuracy) of the test. A robust stability and performance analysis were considered as proposed by Botelho (Botelho 2015). To apply this methodology to aeroRTHS, the VIV was assumed to result in an equivalent negative damping of the physical building model. Therefore, the physical substructure was considered to have various levels of negative damping while still remaining stable.

Fig. 7 shows the robust stability analysis for each of the four aeroelastic flexible-base models considered. The stability results of the building systems given in Table 2 with full damping are shown as solid lines, and the system with reduced damping due to potential VIV negative damping is shown as dashed lines. Robust performance (less than -20 dB) was insured for negative aeroelastic damping of 40% of the inherent damping of the system, namely a damping ratio equal to 0.6% (1.8%), and robust stability (less than 0 dB) was insured for negative aeroelastic damping of 50% of the inherent damping of the system, namely a damping ratio equal to

Table 2. Properties of four tested models

Model	Mass, \tilde{m} (kg)	Damping ratio, ζ (%)	Natural frequency, f_n (Hz)	k_r (N/m)	c_r (kg/s)
FM 1	1.37	1	1.65	147.61	0.28
FM 2	1.37	3	1.65	147.61	0.85
FM 3	2.75	1	1.65	294.92	0.40
FM 4	1.37	3	2.15	250.62	1.57

0.5% (1.5%). Based on the stability and performance analysis, it was determined that the aeroRTHS test would be stable for VIV resulting in aeroelastic damping up to 50% of the inherent damping of structures with accurate results for the test cases considered, and that the aeroRTHS tests could be conducted safely.

Experimental Results

During all aeroRTHS tests, the angle of attack was 0°, and the terrain type was open waterway (Exposure D) (ASCE 2016) with no terraformer raised in the BLWT. The range of testing mean wind velocities was from 0 to 6 m/s, and was measured by a Pitot tube mounted above the building specimen. For each test, the mean wind velocity was kept nearly constant. When employing the aeroRTHS method, the mass, stiffness, and damping of the physical model were prescribed numerically with selected values. Four numerical models with unique dynamic properties were considered to validate the efficacy of the aeroRTHS framework. A model termed the fixed model consisted of the physical building model mounted on the fixed rotational platform. A fixed-based model was equivalent to having the transfer system offline during the test, and is the conventional approach to study interactions between wind and structures in a wind tunnel. The fixed model also was utilized as a reference to compare results from testing models conducted by the aeroRTHS method. These aeroRTHS models in which the transfer system was turned on, were termed the aeroelastic flexible-base models: flexiblebase model 1 (FM1), flexible-base model 2 (FM2), flexible-base model 3 (FM3), and flexible-base model 4 (FM4). Dynamic parameters of these aeroRTHS models are given in Table 2. For the sake of brevity, only dynamic responses of aeroelastic flexible-base models at representative wind speeds are presented here, but all the aeroRTHS testing data have been published and can be downloaded at DesignSafe-CI (Dong et al. 2020), and analysis in greater detail for the first-round aeroRTHS tests was provided by Dong (2021).

In these tests, in order to fully capture the VIV behavior, each aeroRTHS test had a duration of 6 min. The time interval of discretized numerical models was chosen to be 5 ms, which was equal

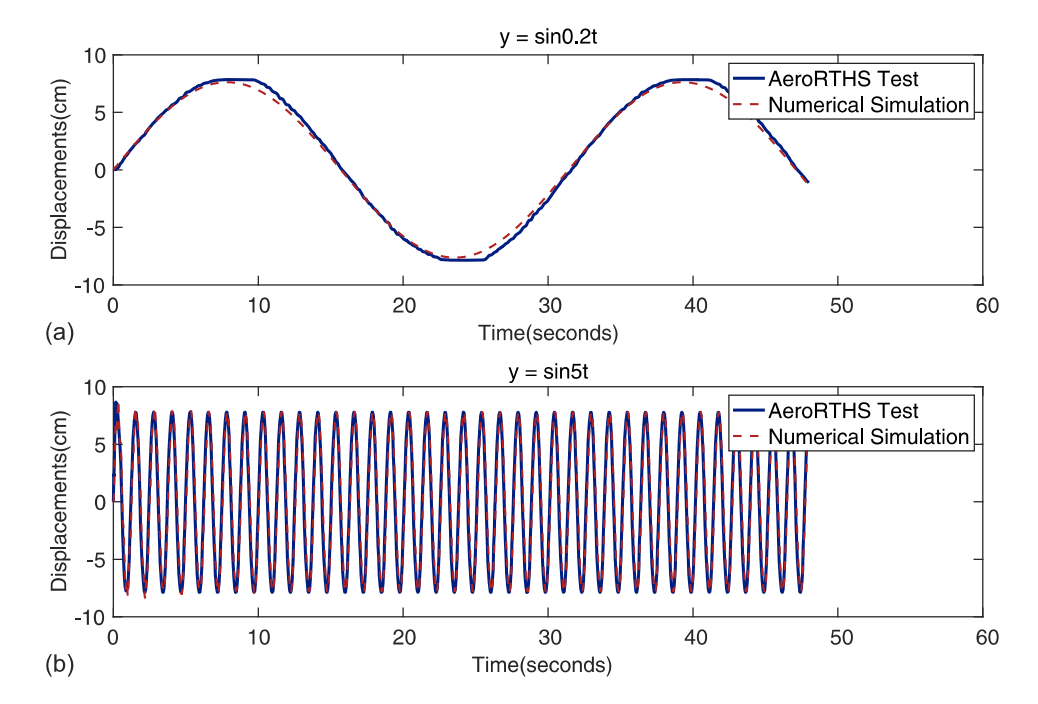


Fig. 8. Pretest for verification purposes: (a) sinusoidal input frequency = 0.03 Hz (0.2 rad/s); and (b) sinusoidal input frequency = 0.8 Hz (5 rad/s).

to the sampling time of measuring surface pressures in Scanivalve system, corresponding to a sampling frequency of 200 Hz. Other sampling times, such as 6, 8, and 10 ms, were investigated; however, pretests showed that results were the most reliable when the position of the physical model was synchronously adjusted with the sampling of the wind pressure.

Verification Test

To demonstrate the aeroRTHS framework, two pretests of aeroRTHS were conducted. Physical structural responses of an aeroelastic flexible-base model excited by numerically generated sinusoidal inputs, f_n , were measured using aeroRTHS and computed purely using numerical simulation. In these tests, no building was subjected

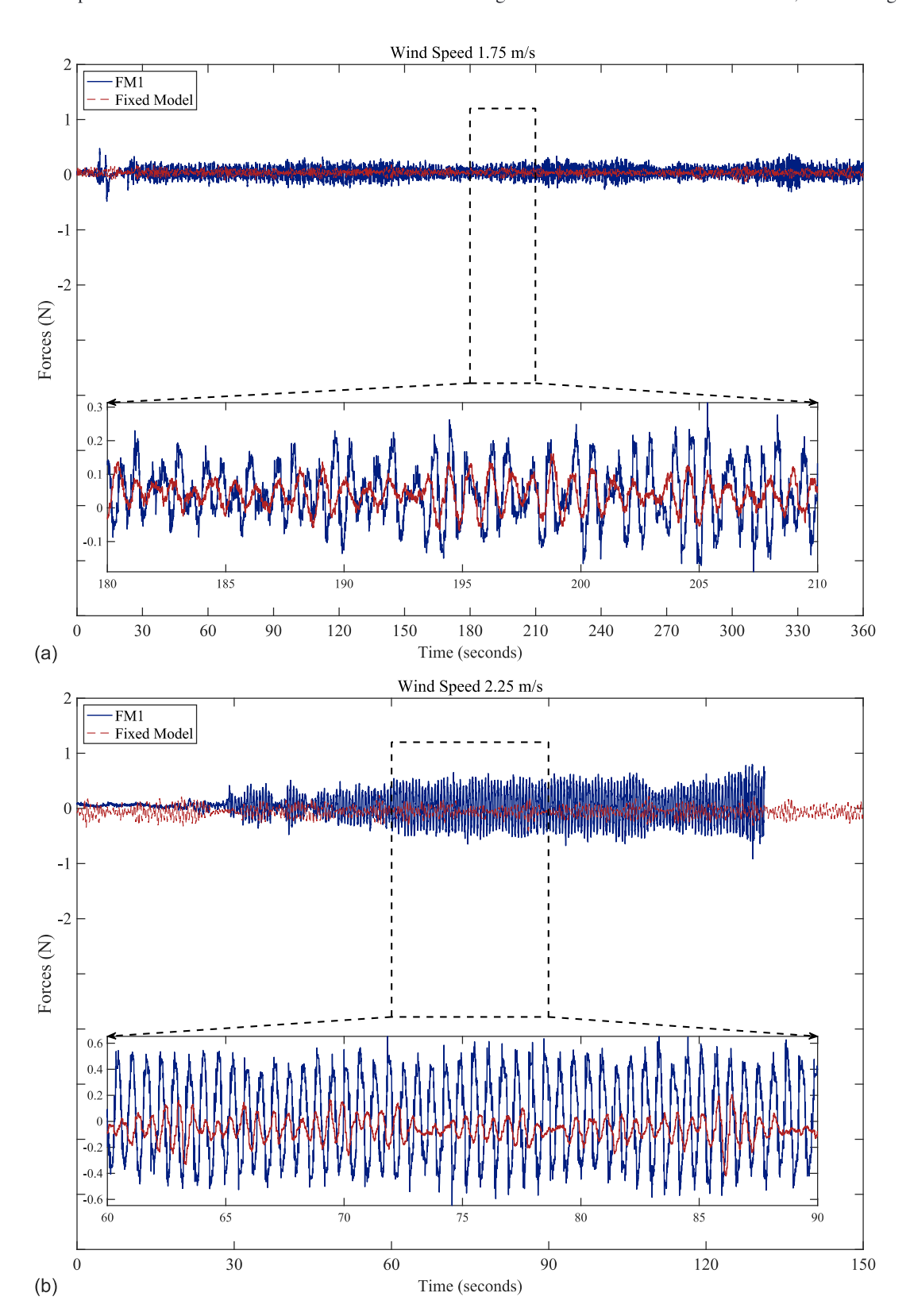


Fig. 9. Equivalent wind forces of the fixed model and FM1 at (a) 1.75 m/s; and (b) 2.25 m/s.

to any cross-wind excitation, and therefore all pressure taps were assumed to provide no pressure or force in the RTHS test. Fig. 8 shows time histories of dynamic displacements of the top of FM1. Fig. 8(a) shows the response due to a sinusoidal input with a frequency of 0.03 Hz (0.2 rad/s), and Fig. 8(b) shows the response under sinusoidal inputs with 0.8 Hz (5 rad/s). Both cases exhibited excellent agreement between the measured and simulated displacements. This verification test confirmed the accuracy of aeroRTHS for conducting dynamic analysis at both extremely low frequency and a frequency near the dynamic of the aeroelastic flexible-base model.

Predicted Critical VIV Wind Speed

Before conducting the tests of the aeroelastic flexible-base models, it was hypothesized that vortex-induced vibrations could be present and could become predominant. A theoretical equation was used to determine the critical wind speeds of vortex-induced vibration for different structures

$$V_{\text{crit}} = \frac{b}{\text{St}} f_n \tag{11}$$

where St = Strouhal number; b = building model's width in the cross-wind direction; and f_n = natural frequency of the numerical model. The Strouhal number is a dimensionless parameter describing oscillating airflow based on the cross-section; 0.12 usually is chosen for sharp-edged square cylinders (Lin et al. 2005; Holmes 2018). Based on a Strouhal number of 0.1, the theoretical critical wind speed to initiate VIV for FM1, FM2, and FM3 was 2.26 m/s, whereas the critical wind speed to initiate VIV for FM4 was 2.95 m/s.

Time Histories of Equivalent Wind Forces

In this section, the dynamic behaviors of four aeroelastic flexible-base models are compared with the results from the fixed model in terms of the equivalent forces. Time histories of forces are plotted to show the total aerodynamic forces of models at three different wind velocities. Effects of changing parameters from FM1, such as the damping ratio (in FM2), the mass (in FM3), and both the damping ratio and natural frequency (in FM4) were investigated.

A total of 65 tests were conducted for 1 fixed model and 4 aeroelastic flexible-base models from 0 to 6 m/s in 0.5 increments. A value of 1.75 m/s was regarded as the low-level wind speed; 2.25 m/s was selected as the critical wind speed of VIV for FM1, FM2, and FM3; 3 m/s was selected as the VIV critical wind speed for FM4; and 6 m/s was considered as the high-level wind speed.

Figs. 9 and 10 show time histories of equivalent forces for FM1 and the fixed model at 1.75, 2.25, and 6 m/s. Similarly, Figs. 11 and 12 show time histories of equivalent forces for FM2 at 1.75, 2.25, and 6 m/s. Fig. 13 shows time histories of equivalent forces for FM3 at 1.75 and 2.25 m/s. Fig. 14 show time histories of equivalent forces for FM4 at 2.25 and 3 m/s.

Fig. 9(a) shows the equivalent forces for FM1 and the fixed model at 1.75 m/s; the solid line indicates the single equivalent wind forces on the tip of FM1, and the dashed line indicates the single equivalent wind forces on the tip of the fixed model. During the entire 6-min test, wind forces of FM1 were slightly larger than those of the fixed model. The magnified image focuses on the time history of forces from 180 to 210 s, which provides more insight. The average value of equivalent forces of FM1 was founded to be 0.086 N. Although 1.75 m/s was treated as the low-level wind speed, FM1 appeared to start experiencing the forced vibrations

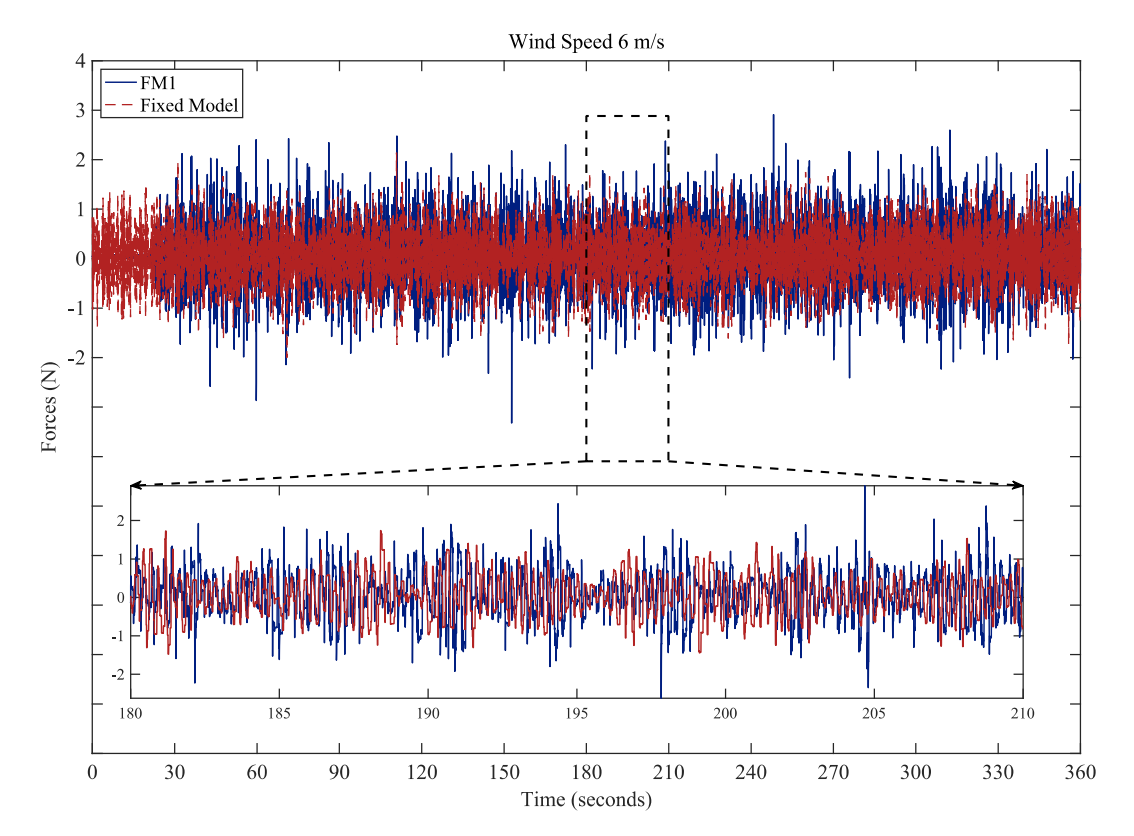


Fig. 10. Equivalent wind forces of the fixed model and FM1 at 6 m/s.

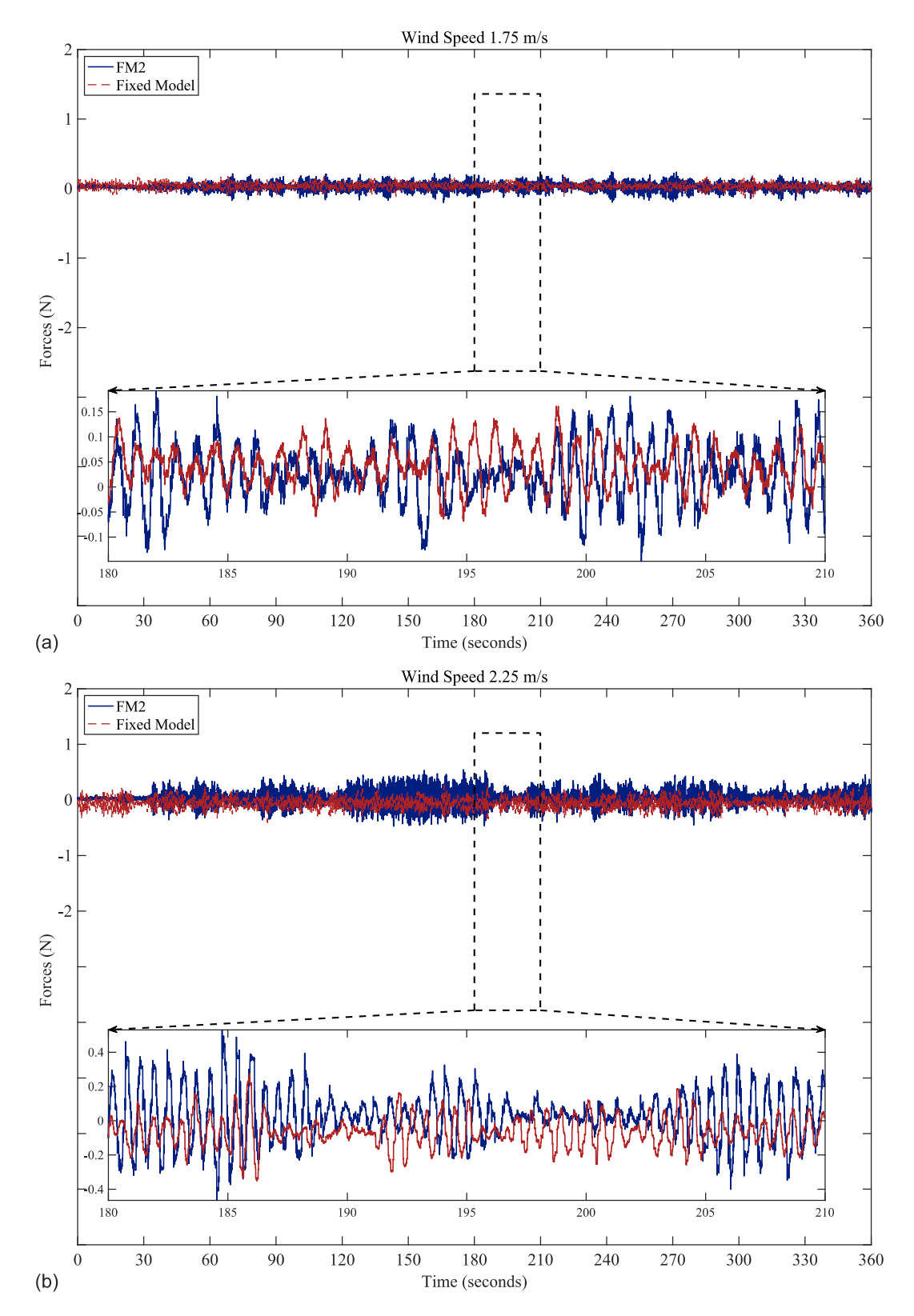


Fig. 11. Equivalent wind forces of the fixed model and FM2 at (a) 1.75 m/s; and (b) 2.25 m/s.

potentially caused by vortices when the wind speed was near the theoretically predicted value, 2.25~m/s (78% of 2.25~m/s); however, the VIV had yet to completely be developed.

Fig. 9(b) shows the equivalent forces for FM1 and the fixed model at 2.25 m/s, which was quite close to the theoretically VIV critical wind speed predicted using Eq. (11). Pronounced differences

between two forces are evident in Fig. 9(b). The mean values of the equivalent forces for the fixed model at 1.75 and 2.25 m/s along with that of FM1 at 1.75 m/s were nearly identical: 0.093, 0.096, and 0.086 N, respectively. However, the average value of the equivalent forces of FM1 was 0.61 N at 2.25 m/s, which was 7 times larger than that at 1.75 m/s. FM1's greatly increased equivalent

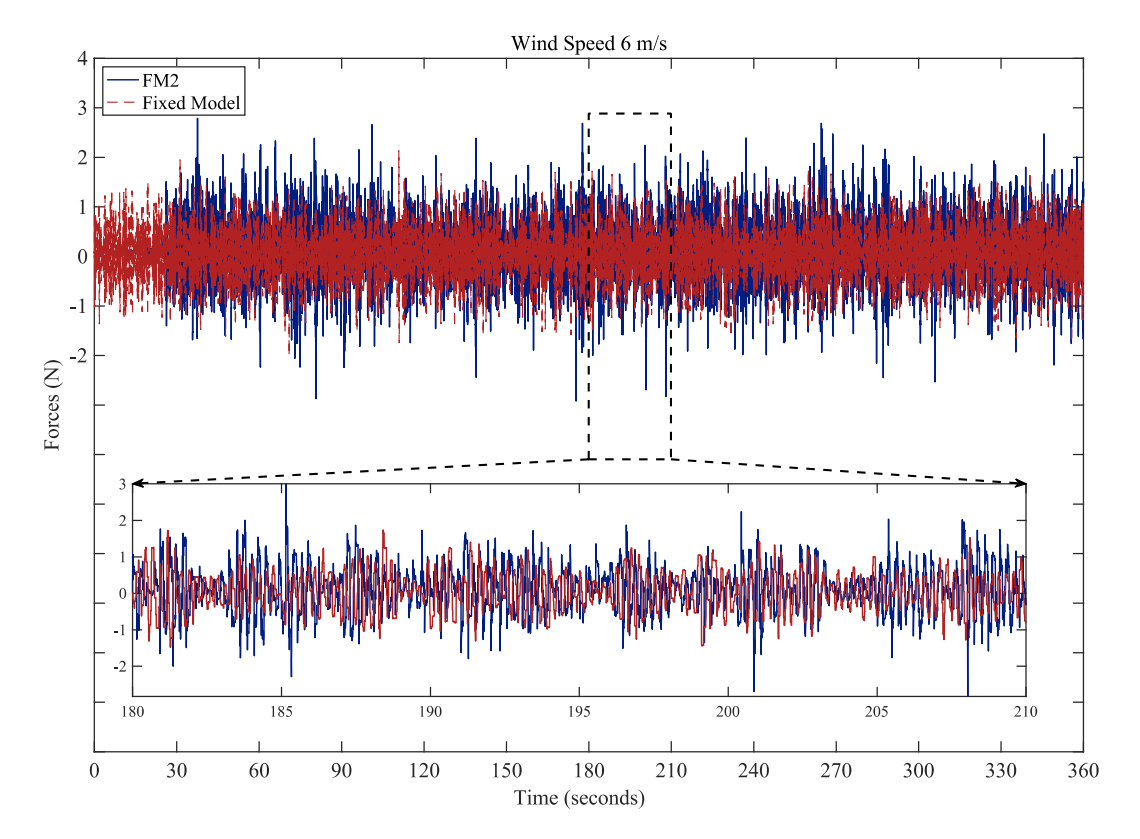


Fig. 12. Equivalent wind forces of the fixed model and FM2 at 6 m/s.

forces at 2.25 m/s demonstrated that aeroRTHS is able to accurately capture the VIV phenomenon.

Fig. 10 shows the equivalent forces of FM1 and the fixed model at 6 m/s. The mean value of equivalent forces of FM1 was 0.84 N at 6 m/s, which was almost the same as that of the fixed model, 0.86 N. There appeared to be no VIV present in their responses at this higher wind speed.

Figs. 11 and 12 show the equivalent forces for FM2 and the fixed model at three wind velocities: 1.75, 2.25, and 6 m/s. The damping ratio was increased from 1% to 3%, and other parameters were unchanged. The theoretical onset of critical wind speed was identical to that for FM1, 2.25 m/s. FM2 with an increased damping ratio had external wind forces with lower magnitudes than those of FM1, and the mean values of equivalent forces were smaller than those of FM1 both at 1.75 and 2.25 m/s. Time histories of forces for FM2 at 2.25 m/s were not notably different from those of FM1; forces first increased and then decreased several times because of the damping effects. It also was observed that the increased damping ratio appeared to mitigate VIV, because the mean magnitude of equivalent forces at the critical wind speed decreased from 0.61 N in FM1 to 0.42 N in FM2. At 6 m/s, and as was the case for FM1, FM2 and the fixed model displayed similar equivalent forces, with a mean value of 0.84 N.

Fig. 13 shows the equivalentits weight was increased to twice that forces for FM3, two times heavier than FM1, and the fixed model. Because FM3 had a greater stiffness, the magnitude of wind forces decreased. Because the damping ratio of FM3 was 1%, identical to that of FM1, the trends of equivalent forces of FM3 were more similar to those of FM1 than to those of FM2 at the low-level and the critical speeds, with mean values of 0.15 and 0.44 N, respectively. The plot for 6 m/s is not shown because the responses were similar to those of FM1 and FM2.

Figs. 14(a and b) show the equivalent forces for FM4 and the fixed model at 2.25 and 3 m/s, respectively. For FM4, the natural frequency changed to 2.15 Hz, and the damping ratio increased to 3%. Instead of discernable variations at 2.25 m/s, wind forces on FM4 were almost identical to those on the fixed model owing to the altered natural frequency. At 3 m/s, as formations of vortices in the wake developed fully, VIV dominated the cross-wind vibration response. The magnitudes of forces also increased greatly compared with those at 2.25 m/s. The plot for 6 m/s is not shown because FM4 had similar behavior to the fixed model; both had a mean value of 0.87 N. Although the wind speed was increased to the highest value used during this set of aeroRTHS tests, wind forces with most significant increase in the cross-wind direction occurred at the specific wind speed predicted by the critical wind speed for VIV.

The comparison of equivalent forces indicates that the aeroRTHS method was able to accurately capture cross-wind vibrations excited by shedding vortices and to easily accommodate multiple dynamic parameters of the building structures with a single physical test specimen.

Time Histories of Displacements

Time histories of displacements at the top floor for four numerical models also were compared. Because the feedback loop of aeroRTHS was offline for the fixed model and a zero displacement command was sent to the transfer system, the displacements for the fixed model were assumed to be zero. Fig. 15 displays the structural responses of the four aeroelastic flexible-base models at 2.25 m/s. FM1, FM2, and FM3 exhibited similar responses. Conversely, FM4, which had a larger natural frequency, 2.15 Hz, manifested different displacement behavior at 2.25 m/s, in which magnitudes of displacements remained nearly constant during the test.

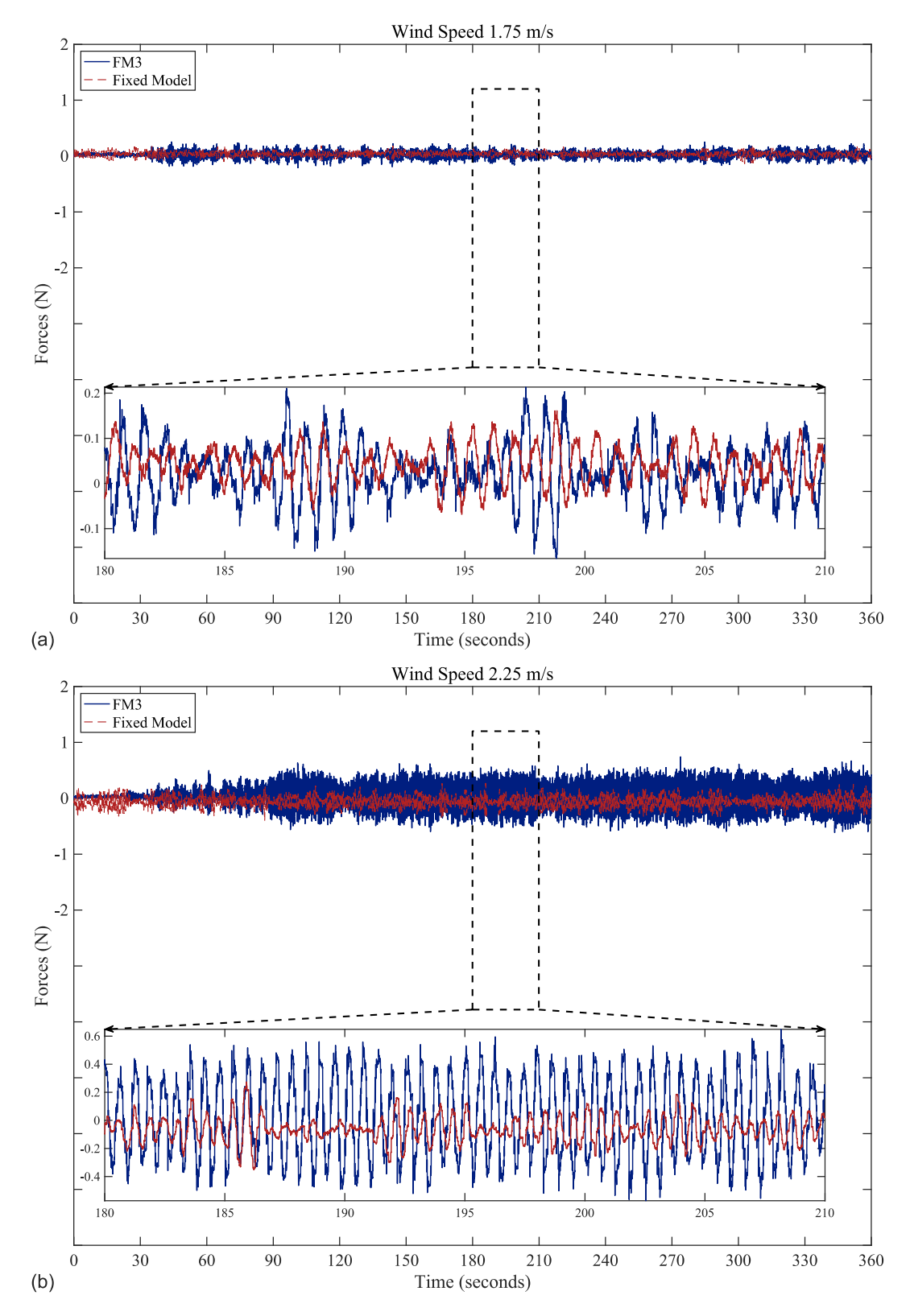


Fig. 13. Equivalent wind forces of the fixed model and FM3 at (a) 1.75 m/s; and (b) 2.25 m/s.

Increasing the damping ratio from 1% (FM1) to 3% (FM2) suppressed VIV, reducing the maximum cross-wind displacements from 20 to 5 cm, but did not eliminate VIV (Fig. 15). The critical wind speeds for those two models nearly coincided with the analytical solutions from Eq. (11). For FM3, three distinct regions were exhibited during VIV: a smooth region at the very beginning

part, a transient regime in which the amplitude increased exponentially, and then a stable stage in which the amplitude of forces remained almost constant for the remainder of the test.

In Fig. 15, time histories of displacements for FM1 are plotted only for the first 130 s because the test was stopped because the safe limit of the shake table was reached. FM2 had similar stages, but

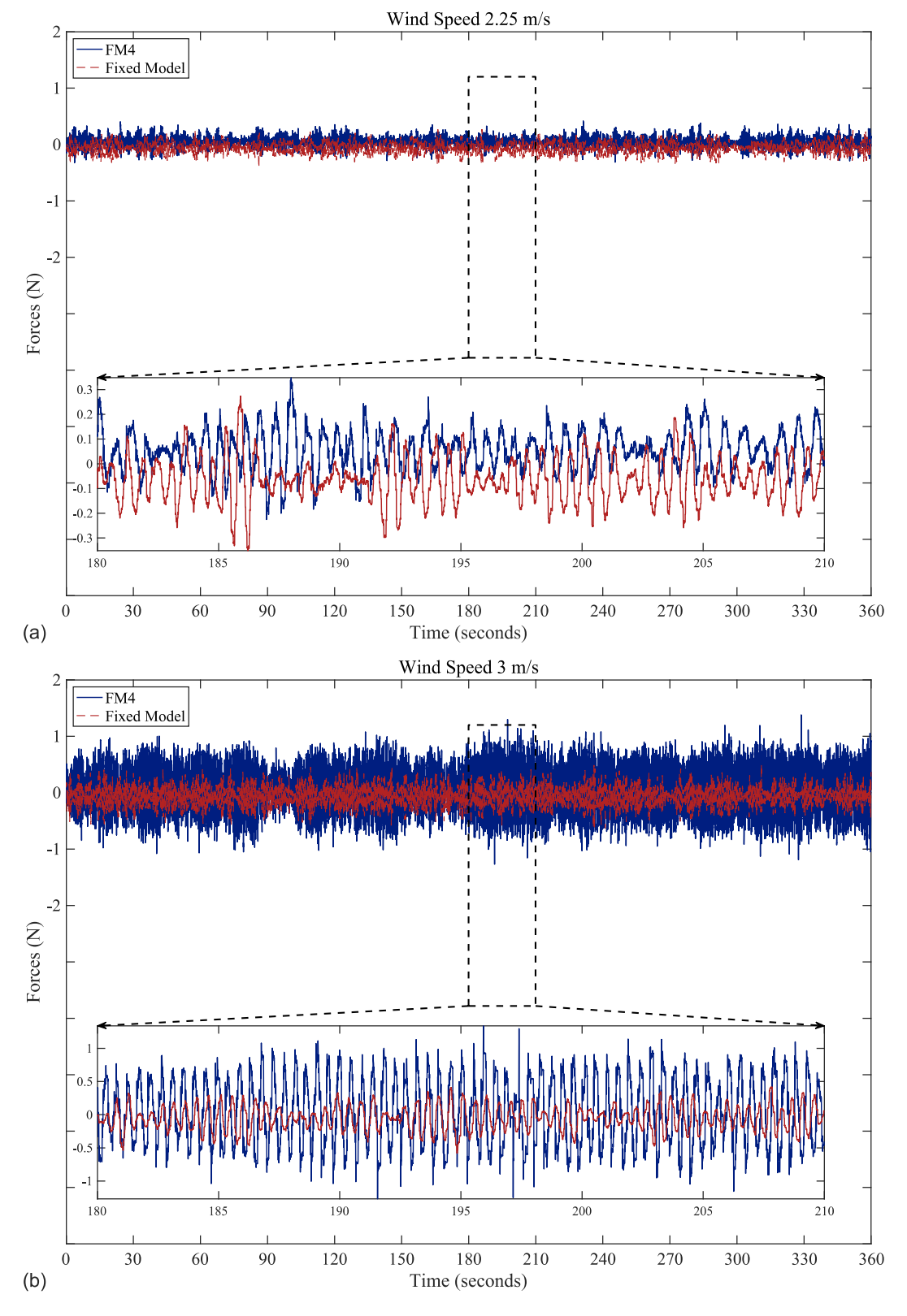


Fig. 14. Equivalent wind forces of the fixed model and FM4 at (a) 2.25 m/s; and (b) 3 m/s.

they were more distinct then in FM1 and FM3 due to the increased damping ratio. The magnitudes of displacements of FM3 were reduced because it became twice as stiff as and had twice the mass of FM1 and FM2, and the threshold of VIV for FM4 varied with the changing fundamental natural frequency. The aeroRTHS captured

these changed dynamic responses, which were not obtainable from the fixed model.

Fig. 16 compares the structural responses of the four aeroelastic flexible-base models at 3 m/s, which was the VIV critical wind speed for FM4. FM4 experienced considerably larger

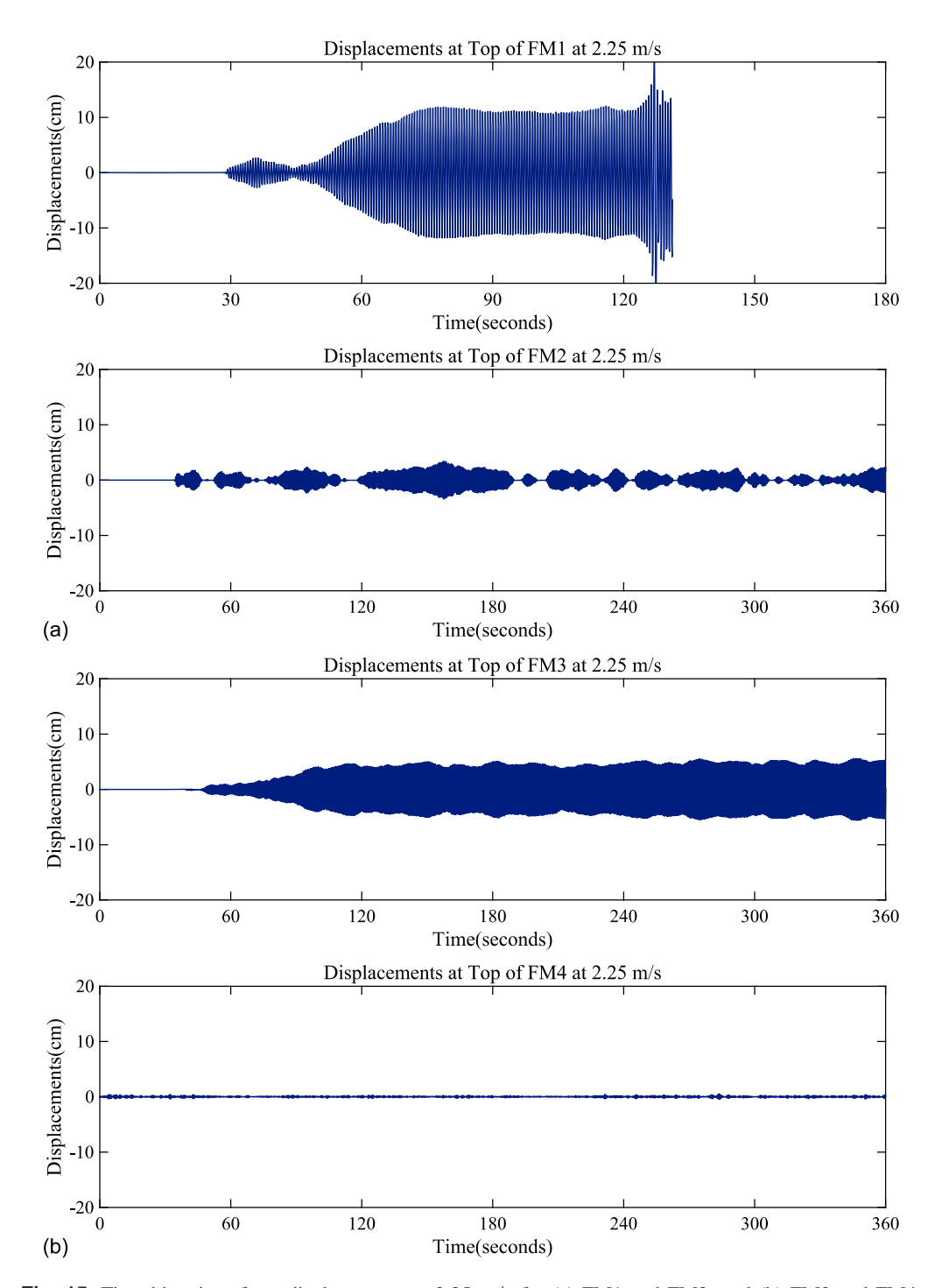


Fig. 15. Time histories of top displacements at 2.25 m/s for (a) FM1 and FM2; and (b) FM3 and FM4.

vibrations than the other three numerical models, as was theoretically predicted.

Resonance at VIV Critical Wind Speed

One reason for excessively dynamic motions of structures under external excitations is the occurrence of resonance. Under the wind loading, the effect of fluid–structure interactions is significant when VIV dominates the cross-wind vibrations. Fig. 17(a) shows time histories of the equivalent force and displacement of FM1 at 2.25 m/s along with 15 cycles of each. From these 15 cycles, the model oscillation frequency (f), vortex shedding frequency for the

building model (f_v) , and the structural natural frequency (f_n) can be computed.

These 15 cycles were selected to calculate the average period for either the model oscillation or the shedding vortices. For the shedding vortices, the starting point of the peak was taken to be at 90.52 s, and the last peak was taken to be at 99.46 s. Correspondingly, for the body oscillation, the starting point of the peak was taken to be at 90.72 s, and the last peak of the 15th cycle was taken to be at 99.73 s. From Eq. (12), f and f_v were almost identical to f_v , 1.65 Hz. The values of f_v and f of FM1 from Fig. 17(a) were calculated to be

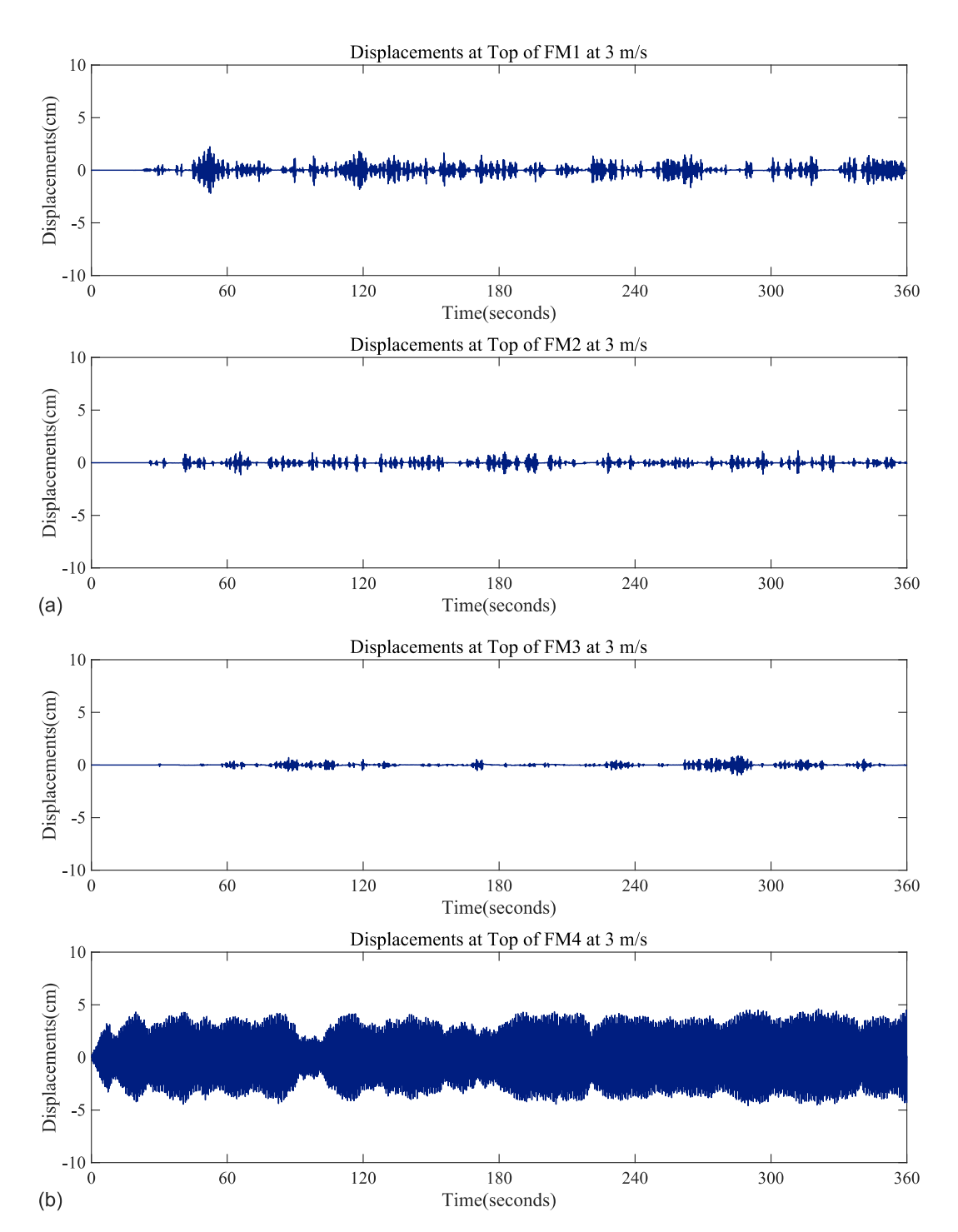


Fig. 16. Time histories of top displacements at 3 m/s for (a) FM1 and FM2; and (b) FM3 and FM4.

$$f_v = \frac{1}{\bar{T}} = \frac{1}{(99.46 - 90.52)/15} = 1.67 \text{ Hz}$$

 $f = \frac{1}{\bar{T}} = \frac{1}{(99.73 - 90.72)/15} = 1.66 \text{ Hz}$ (12)

A similar analysis was repeated for FM2 at 2.25 m/s, FM3 at 2.25 m/s, and FM4 at 3 m/s with time histories in Figs. 17(b) and 18(a and b) used to compute the model oscillation frequency and the shedding vortex frequencies in Eqs. (13)–(15), respectively. For these additional models, it similarly was found that f and f_v had good agreement with f_n .

For FM2 [Fig. 17(b)]

$$f_v = \frac{1}{\bar{T}} = \frac{1}{(159.585 - 150.62)/15} = 1.67 \text{ Hz}$$

$$f = \frac{1}{\bar{T}} = \frac{1}{(159.8 - 150.27)/16} = 1.67 \text{ Hz}$$
(13)

For FM3 [Fig. 18(a)]

$$f_v = \frac{1}{\bar{T}} = \frac{1}{(159.505 - 150.55)/15} = 1.67 \text{ Hz}$$

$$f = \frac{1}{\bar{T}} = \frac{1}{(159.715 - 150.12)/16} = 1.66 \text{ Hz}$$
(14)

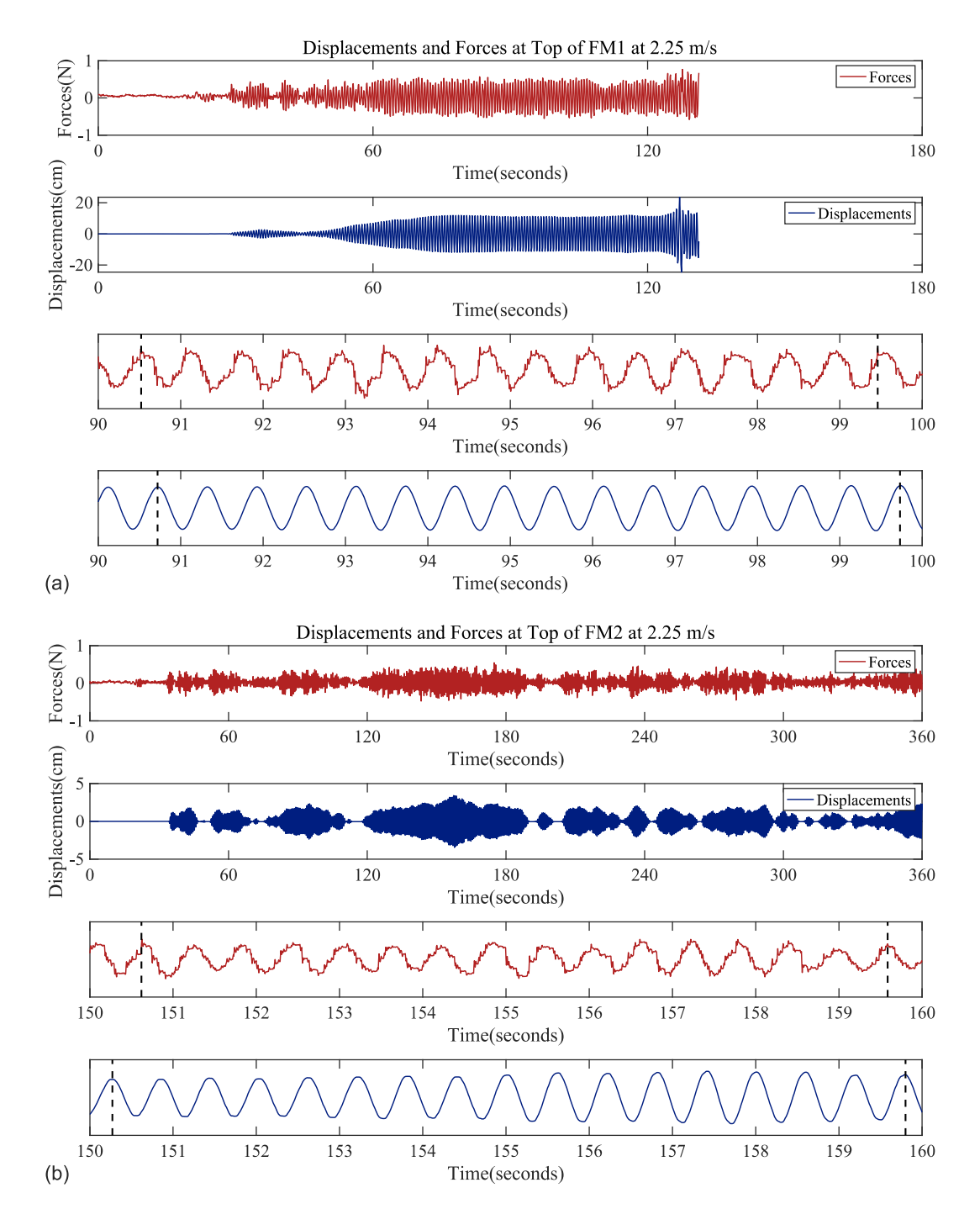


Fig. 17. Time histories of top equivalent wind forces and top displacements (a) at 2.25 m/s for FM3; and (b) at 3 m/s for FM4.

For FM4 [Fig. 18(b)]

$$f_v = \frac{1}{\bar{T}} = \frac{1}{(159.59 - 150.255)/20} = 2.14 \text{ Hz}$$

$$f = \frac{1}{\bar{T}} = \frac{1}{(159.68 - 150.44)/20} = 2.16 \text{ Hz}$$
(15)

A wind velocity sweep test also was conducted for FM4 from 1.5 to 6 m/s, and the results are shown in Fig. 19 for the equivalent forces and top displacements. The VIV was observed from 90 to 120 s of the test when the wind speed was about 3 m/s.

The equivalent forces were synchronized with time histories of displacements but were out of phase by 180°. FM4 experienced three noticeable stages during the sweep wind test. Both top displacements and equivalent forces of FM4 were small when the wind velocity was low, and then with an appropriate increase of the wind forces and the wind speed, the transverse displacements were significantly increased due to the occurrence of VIV. In the last stage, the aerodynamic forces continued to increase as the wind velocity increased, but transverse displacements were reduced because the VIV phenomenon ended. Fig. 19(b) shows the displacements from 100 to 110 s [within the dashed rectangle in Fig. 19(a)] to highlight the behavior during the suspected VIV.

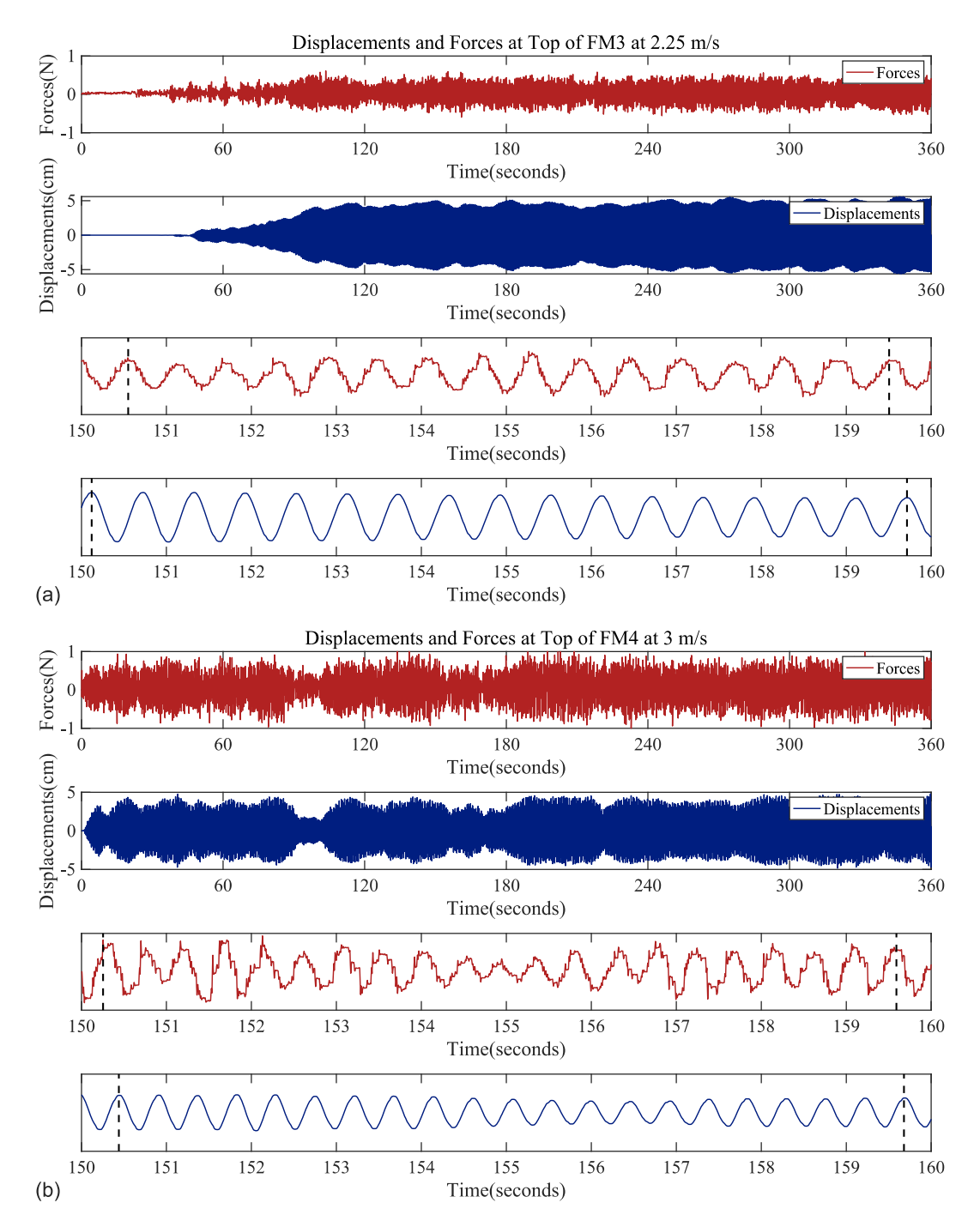


Fig. 18. Time histories of top equivalent wind forces and top displacements (a) at 2.25 m/s for FM3; and (b) at 3 m/s for FM4.

Standard Deviations of Equivalent Wind Forces and Displacements

Standard deviations of displacements at the top for four models were computed. Again, changes in parameters of the numerical model altered the cross-wind response, which cannot be detected if only a fixed model was utilized in the BLWT.

For FM1, there was a testing gap between 1.5 and 2.25 m/s because oscillations of FM1 exceeded the safety limit of the shake table [Fig. 20(a)]. FM1 had the largest dynamic response due to its small damping ratio; by changing the damping ratio from 1% to 3%, the dynamic response of FM2 was significantly reduced; the dynamic motions of FM3 also decreased, and the model became

stiffer than the other three aeroelastic flexible-base models because its weight was increased to twice that of FM1. The threshold of critical wind speed was 3 m/s for FM4 with a 2.15 Hz natural frequency, and its σ value of top displacements decreased.

For the peak spectral displacement, Welch's power spectral density was utilized to estimate the strength of displacement at different frequencies; the largest power spectral density of displacements (the peak spectral displacement) was obtained to provide a comprehensive perspective on the VIV phenomenon in terms of the maximum energy and power at each wind speed. Fig. 20(b) demonstrates the relation between wind velocities and the peak spectral displacements in the frequency domain; the energy was a function of wind

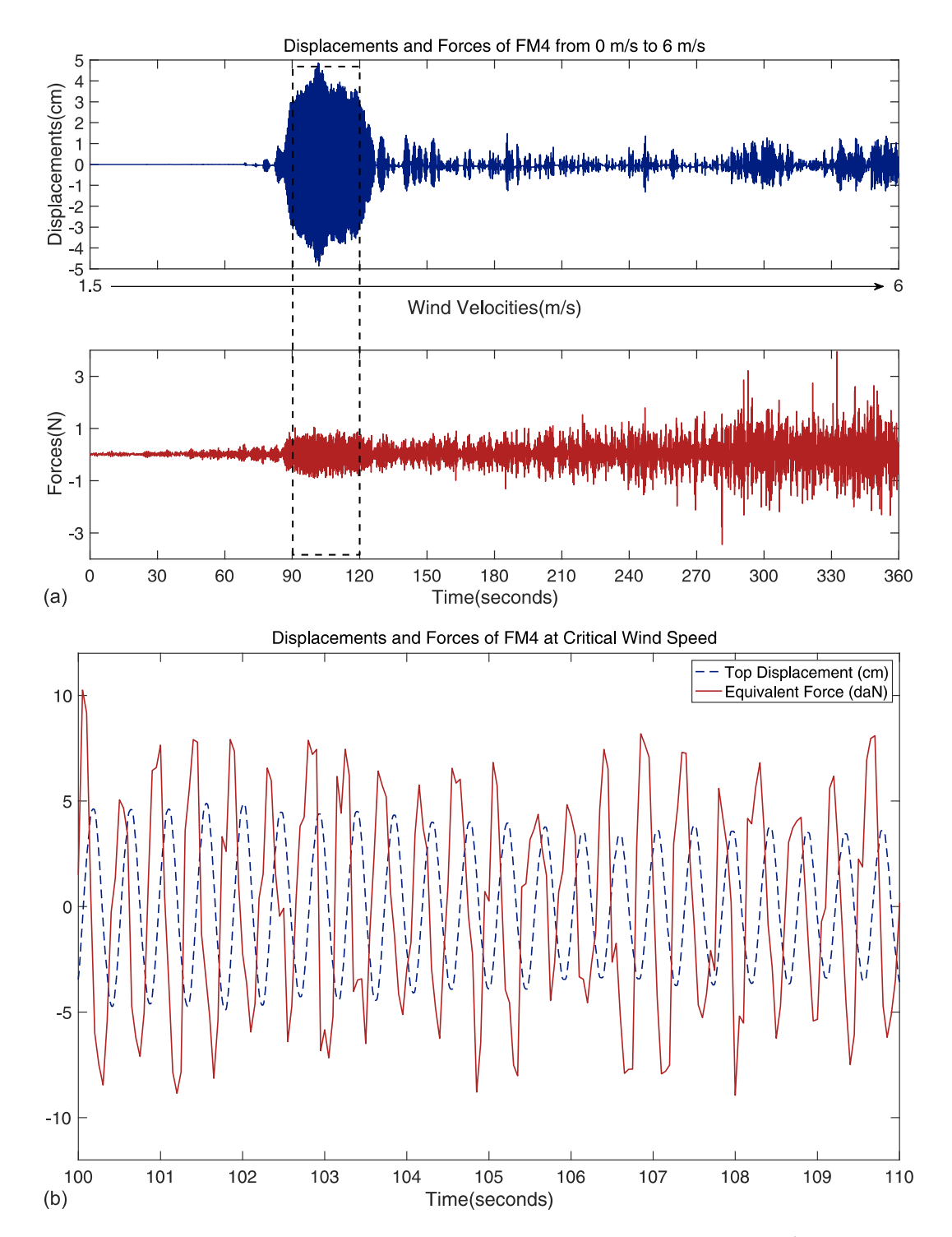


Fig. 19. Time histories of cross-wind displacements and equivalent wind forces of FM4 (a) from 0 to 6 m/s; and (b) from 100 to 110 s.

speed for all models. Fig. 20(b) has the same trend as Fig. 20(a): the strength of release energy for a building structure was the largest at the VIV.

Fig. 21 shows the standard deviation of equivalent forces as a function of increasing wind velocity; the reference line indicates aerodynamic forces as a function of the square of the wind speed, which is a simplified approach to estimate wind loading as static forces in the design stage. The curve of the standard deviation of wind forces for the fixed model coincides with that of the reference

line because neither the fixed model nor the reference takes into account fluid-structure interaction.

The impact of cross-wind vibrations on flexible building structures was underestimated at critical wind speeds by the conventional method, which treated the testing specimen as a rigid system by ignoring the effects of fluid–structure interaction. However, the simplified method overestimated the aerodynamic impact on structures when the wind speed was higher than the critical wind speed.

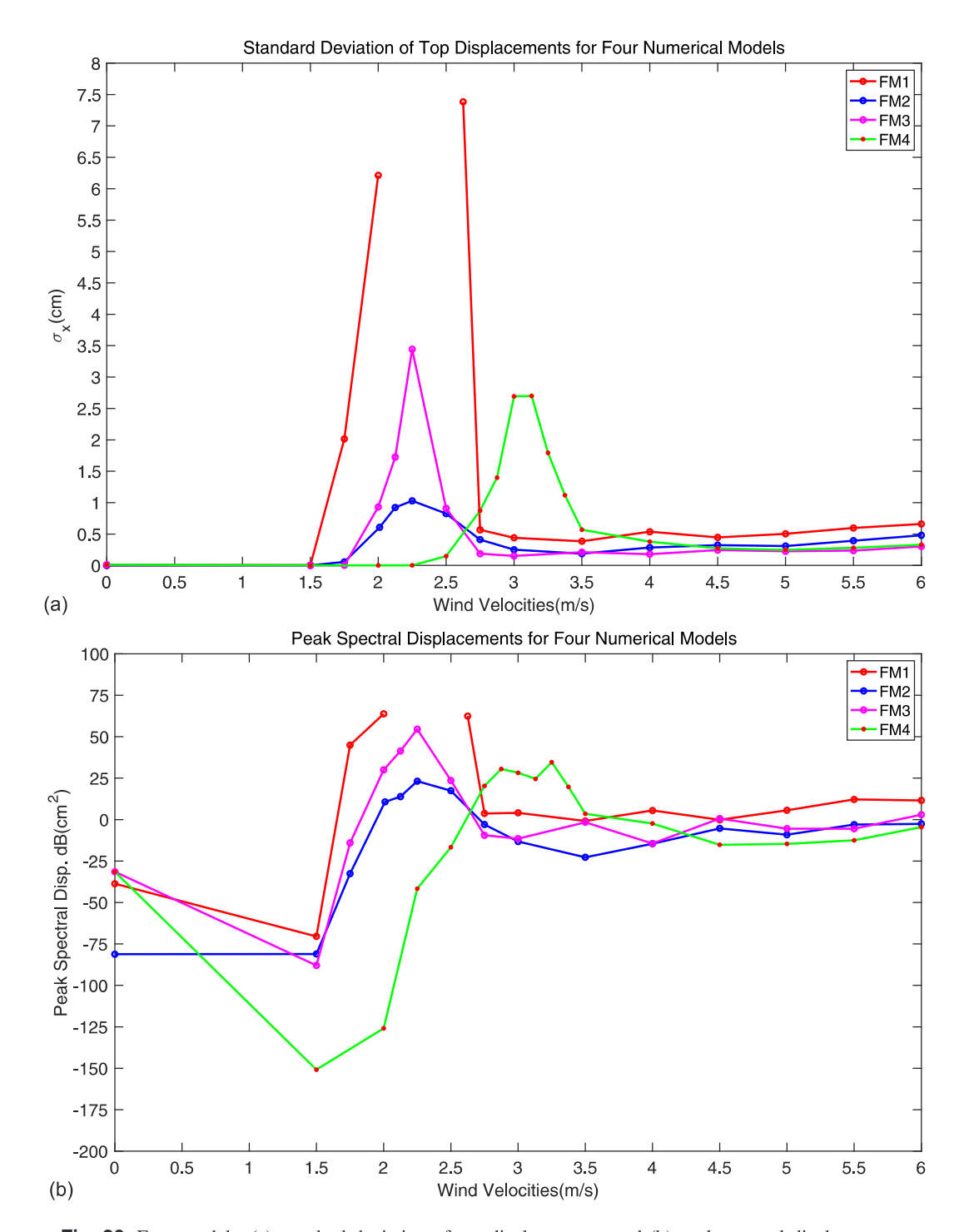


Fig. 20. Four models: (a) standard deviation of top displacements; and (b) peak spectral displacements.

Conclusions and Future Work

The results from a series of proof-of-concept tests demonstrated the feasibility of the aeroRTHS method. It was shown that the compensation of a transfer system between the numerical and experimental substructures, as well as the compensation and calculation of single equivalent force from multiple pressure sensors, could be achieved under real-time conditions with a sampling frequency of 200 Hz. Moreover, it was demonstrated that the aeroRTHS method easily can accommodate the varying of dynamic model parameters such as the damping ratio, mass, and the natural frequency of the numerical substructure, allowing for a wide array of buildings to be

analyzed using a single physical model. Notable differences between forces applied to and displacement responses of the fixed-base model and aeroelastic flexible-base models were observed, providing further evidence of the aeroRTHS method's ability to capture fluid-structure interaction. Finally, it was demonstrated that the body oscillating frequency (f), the vortex shedding frequency (f), and the natural frequency (f) all coincided when the models were excited at the critical wind speed, providing evidence that the proposed methodology can capture vortex-induced vibrations accurately. The companion paper (Dong et al., forthcoming) discusses results from a second round of aeroRTHS testing in 2018 at UF BLWT, in which the approach discussed herein is expanded in

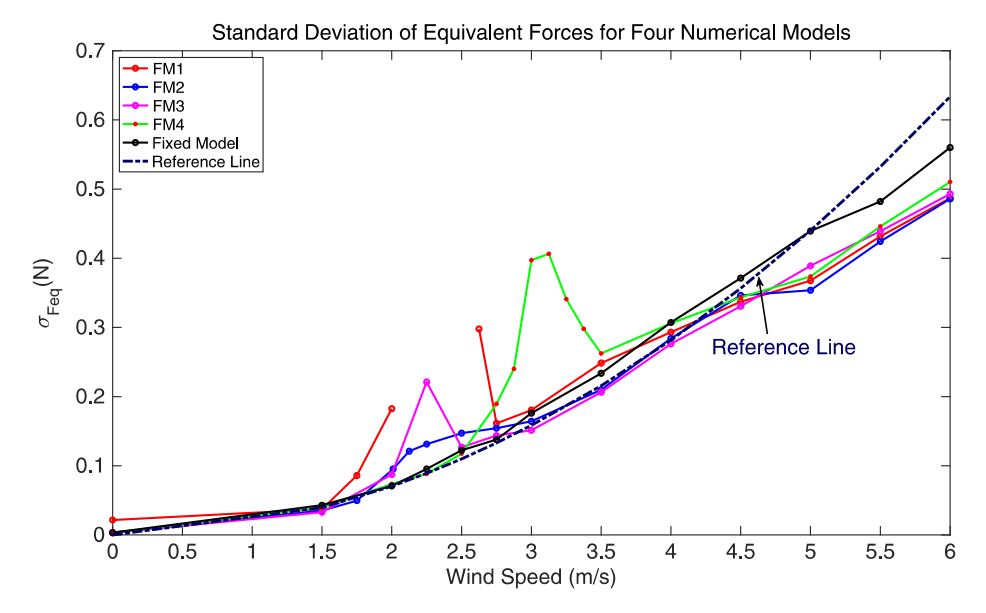


Fig. 21. Standard deviation of equivalent wind forces for four models

multiple aspects: (1) a vibration control device is added numerically and tested to mitigate the cross-wind oscillation for different numerical models using the aeroRTHS framework; and (2) a detailed characterization is given of the wind loading acting on the physical building model, including power spectral density of equivalent forces and displacements and the distribution of wind forces at different vertical levels in terms of mean wind force contours and extreme values at cross-wind surfaces.

Data Availability Statement

Some or all data, models, or code generated or used during the study are available in a repository online in accordance with funder data retention policies at https://doi.org/10.17603/ds2-zxwk-2f93.

Acknowledgments

The authors gratefully acknowledge the support of this work by the National Science Foundation through Award CMMI-1732223 (Clarkson University) and CMMI-1732213 (University of Connecticut). The NSF NHERI Experimental Facility that contributed to the research results reported within this paper was supported under NSF Award 1520843. Any opinions, findings, and conclusions expressed herein are those of the authors and do not necessarily reflect the views of the National Science Foundation.

References

Aboutabikh, M., A. Elshaer, and H. Aboshosha. 2022. "A low-cost expandable multi-channel pressure system for wind tunnels." Wind Struct. 35 (5): 297–307. https://doi.org/10.12989/was.2022.35.5.297.

Amezquita-Sanchez, J. P., H. S. Park, and H. Adeli. 2017. "A novel methodology for modal parameters identification of large smart structures using MUSIC, empirical wavelet transform, and Hilbert transform." Eng. Struct. 147 (Sep): 148–159. https://doi.org/10.1016/j.engstruct.2017.05.054.

Amin, J. A., and A. K. Ahuja. 2014. "Characteristics of wind forces and responses of rectangular tall buildings." *Int. J. Adv. Struct. Eng.* 6 (3): 1. https://doi.org/10.1007/s40091-014-0066-1. ASCE. 2016. Minimum design loads and associated criteria for buildings and other structures. ASCE 7-16. Reston, VA: ASCE.

Aurenhammer, F. 1991. "Voronoi diagrams—A survey of a fundamental geometric data structure." *ACM Comput. Surv.* 23 (3): 345–405. https://doi.org/10.1145/116873.116880.

Bashor, R., S. Bobby, T. Kijewski-Correa, and A. Kareem. 2012. "Full-scale performance evaluation of tall buildings under wind." *J. Wind Eng. Ind. Aerodyn.* 104–106 (May–Jul): 88–97. https://doi.org/10.1016/j.jweia.2012.04.007.

Bendat, J. S., and A. G. Piersol. 2010. Random data: Analysis and measurement procedures. Hoboken, NJ: Wiley.

Blocken, B. 2014. "50 years of computational wind engineering: Past, present and future." *J. Wind Eng. Ind. Aerodyn.* 129 (Jun): 69–102. https://doi.org/10.1016/j.jweia.2014.03.008.

Blocken, B., and J. Carmeliet. 2004. "Pedestrian wind environment around buildings: Literature review and practical examples." J. Therm. Envelope Build. Sci. 28 (2): 107–159. https://doi.org/10.1177/1097196304044396.

Blocken, B., D. Derome, and J. Carmeliet. 2013. "Rainwater runoff from building facades: A review." *Build. Environ.* 60 (Feb): 339–361. https://doi.org/10.1016/j.buildenv.2012.10.008.

Botelho, R. M. 2015. "Real-time hybrid substructuring for marine applications of vibration control and structural acoustics." Ph.D. thesis, Dept. of Civil and Environmental Engineering, Univ. of Connecticut.

Carrion, J. E. 2008. Model-based strategies for real-time hybrid testing. Newmark Structural Engineering Laboratory Report 1940-9826. Champaign, IL: Newmark Structural Engineering Laboratory, Univ. of Illinois at Urbana-Champaign.

Catarelli, R. A., P. L. Fernández-Cabán, F. J. Masters, J. A. Bridge, K. R. Gurley, and C. J. Matyas. 2020a. "Automated terrain generation for precise atmospheric boundary layer simulation in the wind tunnel." *J. Wind Eng. Ind. Aerodyn.* 207 (Dec): 104276. https://doi.org/10.1016/j.jweia.2020.104276.

Catarelli, R. A., P. L. Fernández-Cabán, B. M. Phillips, J. A. Bridge, F. J. Masters, K. R. Gurley, and D. O. Prevatt. 2020b. "Automation and new capabilities in the University of Florida NHERI Boundary Layer Wind Tunnel." Front. Built Environ. 6: 558151. https://doi.org/10.3389/fbuil.2020.558151.

Cermak, J. E. 1995. "Progress in physical modeling for wind engineering." *J. Wind Eng. Ind. Aerodyn.* 54–55: 439–455. https://doi.org/10.1016/0167-6105(94)00064-K.

Cermak, J. E. 2003. "Wind-tunnel development and trends in applications to civil engineering." *J. Wind Eng. Ind. Aerodyn.* 91 (3): 355–370. https://doi.org/10.1016/S0167-6105(02)00396-3.

- Chen, Z. S., Y. M. Xu, H. L. Huang, and K. T. Tse. 2020. "Wind tunnel measurement systems for unsteady aerodynamic forces on bluff bodies: Review and new perspective." Sensors 20 (16): 32824586. https://doi.org/10.3390/s20164633.
- Choi, E. C. C. 1993. "Simulation of wind-driven-rain around a building." J. Wind Eng. Ind. Aerodyn. 46–47 (Aug): 721–729. https://doi.org/10.1016/0167-6105(93)90342-L.
- Christenson, R., Y. Z. Lin, A. Emmons, and B. Bass. 2008. "Large-scale experimental verification of semiactive control through real-time hybrid simulation." *J. Struct. Eng.* 134 (4): 522–534. https://doi.org/10.1061/(ASCE)0733-9445(2008)134:4(522).
- Darby, A. P., A. Blakeborough, and M. S. Williams. 1999. "Real-time substructure tests using hydraulic actuator." *J. Eng. Mech.* 125 (10): 1133–1139. https://doi.org/10.1061/(ASCE)0733-9399(1999)125: 10(1133).
- Davenport, A. G. 1967. "The treatment of wind loading on tall buildings." In *Tall buildings*. Amsterdam, Netherlands: Elsevier.
- Dermitzakis, S. N., and S. A. Mahin. 1985. Development of substructuring techniques for on-line computer controlled seismic performance testing. Rep. No. UCB/EERC-85/04. Berkeley, CA: Univ. of California, Berkeley.
- Dong, J. 2021. "Aeroelastic real-time hybrid simulation (aeroRTHS): Validation and mitigation of vortex induced vibration of a tall building structure." Ph.D. thesis, Dept. of Civil and Environmental Engineering, Clarkson Univ.
- Dong, J., S. Lobo-Aguilar, Y. Yuan, S. Wojtkiewicz, and R. Christenson. 2020. "Aeroelastic real-time hybrid simulation (2017 and 2018 tests at University of Florida NHERI EF)." https://doi.org/10.17603/ds2-zxwk -2f93.
- Dong, J., S. Wojtkiewicz, and R. Christenson. Forthcoming. "Aeroelastic real-time hybrid simulation. II: Mitigation of vortex induced vibration of a tall building structure." *J. Eng. Mech.* 150 (9): 04024061. https:// doi.org/10.1061/JENMDT/EMENG-7159.
- Dragoiescu, C., J. Garber, and K. S. Kumar. 2006. "A comparison of force balance and pressure integration techniques for predicting wind-induced responses of tall buildings." In *Proc.*, *Structures Congress 2006: Structural Engineering and Public Safety*, 1–10. Reston, VA: ASCE.
- Gerstoft, P., and S. O. Hansen. 1987. "A new tubing system for the measurement of fluctuating pressures." *J. Wind Eng. Ind. Aerodyn.* 25 (3): 335–354. https://doi.org/10.1016/0167-6105(87)90026-2.
- Gierson, M. L., B. M. Phillips, D. Duthinh, and B. M. Ayyub. 2017. "Wind-pressure coefficients on low-rise building enclosures using modern wind-tunnel data and Voronoi diagrams." ASCE-ASME J. Risk Uncertainty Eng. Syst., Part A: Civ. Eng. 3 (4): 04017010. https://doi.org/10.1061/AJRUA6.0000915.
- Gu, M., and Y. Quan. 2004. "Across-wind loads of typical tall buildings." J. Wind Eng. Ind. Aerodyn. 92 (13): 1147–1165. https://doi.org/10.1016/j.jweia.2004.06.004.
- Guibas, L., and J. Stolfi. 1985. "Primitives for the manipulation of general subdivisions and the computation of Voronoi." ACM Trans. Graphics 4 (2): 74–123. https://doi.org/10.1145/282918.282923.
- Hakuno, M., M. Shidawara, and T. Hara. 1969. "Dynamic destructive test of a cantilever beam, controlled by an analog-computer." In Vol. 1969 of *Proc. Japan Society of Civil Engineers*, 1–9. Tokyo: Japan Society of Civil Engineers. https://doi.org/10.2208/jscej1969.1969.171_1.
- Holmes, J. D. 2018. Wind loading of structures. Milton Park, UK: Taylor & Francis.
- Holmes, J. D., A. Rofail, and L. Aurelius. 2003. "High frequency base balance methodologies for tall buildings with torsional and coupled resonant modes." In *Proc.*, 11th Int. Conf. on Wind Engineering, 2381–2388. Bochum, Germany: International Association for Wind Engineering.
- Holmes, J. D., and K. T. Tse. 2014. "International high-frequency base balance benchmark study." *Wind Struct.* 18 (4): 457–471. https://doi.org/10.12989/was.2014.18.4.457.
- Jung, R. Y., and P. B. Shing. 2006. "Performance evaluation of a real-time pseudodynamic test system." *Earthquake Eng. Struct. Dyn.* 35 (7): 789–810. https://doi.org/10.1002/eqe.547.
- Kanda, M. 1995. "Development of hybrid experimental system combined with random response analysis for unsteady aerodynamic vibration of

- structure." In *Proc.*, 9th Int. Conf. on Wind Engineering. Bochum, Germany: International Association for Wind Engineering.
- Kanda, M., A. Kawaguchi, T. Koizumi, and E. Maruta. 2003. "A new approach for simulating aerodynamic vibrations of structures in a wind tunnel—Development of an experimental system by means of hybrid vibration technique." J. Wind Eng. Ind. Aerodyn. 91 (11): 1419–1440. https://doi.org/10.1016/j.jweia.2003.07.002.
- Kato, N., T. Ohkuma, J. R. Kim, H. Marukawa, and Y. Niihori. 1992. "Full scale measurements of wind velocity in two urban areas using an ultrasonic anemometer." *J. Wind Eng. Ind. Aerodyn.* 41 (1–3): 67–78. https://doi.org/10.1016/0167-6105(92)90394-P.
- Kato, Y., and M. Kanda. 2014. "Development of a modified hybrid aerodynamic vibration technique for simulating aerodynamic vibration of structures in a wind tunnel." J. Wind Eng. Ind. Aerodyn. 135 (Dec): 10–21. https://doi.org/10.1016/j.jweia.2014.09.005.
- Kawaguchi, A., M. Kanda, E. Maruta, and T. Koizumi. 2001. "Elasto-plastic behavior of square prisms under wind loading—Application of hybrid vibration system in wind tunnel tests." J. Wind Eng. 89: 89–92.
- Kawaguchi, A., E. Maruta, and M. Kanda. 1999. "Hybrid vibration system for evaluation of wind force on structures." In *Proc.*, 10th Int. Conf. on Wind Engineering, 455–460. Bochum, Germany: International Association for Wind Engineering.
- Kijewski-Correa, T., D. K. Kwon, A. Kareem, A. Bentz, Y. Guo, S. Bobby, and A. Abdelrazaq. 2012. "SmartSync: An integrated real-time structural health monitoring and structural identification system for tall buildings." J. Struct. Eng. 139 (10): 1675–1687. https://doi.org/10.1061/(ASCE)ST.1943-541X.0000560.
- Kilpatrick, J., et al. 2003. "Full scale validation of the predicted response of tall buildings: Preliminary results of the Chicago monitoring project." In *Proc. 11th Int. Conf. on Wind Engineering*, 2–5. Bochum, Germany: International Association for Wind Engineering.
- Li, Q. S., J. Q. Fang, A. P. Jeary, and C. K. Wong. 1998. "Full-scale measurements of wind effects on tall buildings." *J. Wind Eng. Ind. Aerodyn.* 74 (Apr): 741–750. https://doi.org/10.1016/S0167-6105(98)00067-1.
- Li, Q. S., Y. Q. Xiao, J. Y. Fu, and Z. N. Li. 2007. "Full-scale measurements of wind effects on the Jin Mao building." *J. Wind Eng. Ind. Aerodyn.* 95 (6): 445–466. https://doi.org/10.1016/j.jweia.2006.09.002.
- Li, Q. S., Y. Q. Xiao, J. R. Wu, J. Y. Fu, and Z. N. Li. 2008. "Typhoon effects on super-tall buildings." *J. Sound Vib.* 313 (3–5): 581–602. https://doi.org/10.1016/j.jsv.2007.11.059.
- Li, Q. S., L. H. Zhi, J. Yi, A. To, and J. Xie. 2014. "Monitoring of typhoon effects on a super-tall building in Hong Kong." *Struct. Control Health Monit.* 21 (6): 926–949. https://doi.org/10.1002/stc.1622.
- Lin, N., C. Letchford, Y. Tamura, B. Liang, and O. Nakamura. 2005. "Characteristics of wind forces acting on tall buildings." *J. Wind Eng. Ind. Aerodyn.* 93 (3): 217–242. https://doi.org/10.1016/j.jweia.2004.12.001.
- Melbourne, W. H. 1977. "Probability distributions associated with the wind loading structures." *Inst. Eng. (Aust.) Civ. Eng. Trans.* 1: 58–67.
- Mochida, A., and I. Y. F. Lun. 2008. "Prediction of wind environment and thermal comfort at pedestrian level in urban area." *J. Wind Eng. Ind. Aerodyn.* 96 (10–11): 1498–1527. https://doi.org/10.1016/j.jweia.2008.02.033.
- Nakata, N., et al. 2014. "Hybrid simulation primer and dictionary." *Network Earthquake Eng. Simul.* Alexandria, VA: US National Science Foundation.
- Nishi, M., and M. Kanda. 2010. "Application of hybrid experimental technique for simulating aerodynamic vibration of structures in a wind tunnel." In *Proc.*, 5th Int. Symp. on Computational Wind Engineering, 455–460. Bochum, Germany: International Association for Wind Engineering.
- Norton, T., D. W. Sun, J. Grant, R. Fallon, and V. Dodd. 2007. "Applications of computational fluid dynamics (CFD) in the modelling and design of ventilation systems in the agricultural industry: A review." *Bioresour. Technol.* 98 (12): 2386–2414. https://doi.org/10.1016/j.biortech.2006.11.025.
- Pemberton, R. 2010. An overview of dynamic pressure measurement considerations. Liberty Lake, WA: Scanivalve.
- Reichrath, S., and T. W. Davies. 2002. "Using CFD to model the internal climate of greenhouses: Past, present and future." *Agronomie* 22 (1): 3–19. https://doi.org/10.1051/agro:2001006.

- Shing, P. B., M. Nakashima, and O. S. Bursi. 1996. "Application of pseudodynamic test method to structural research." *Earthquake Spectra* 12 (1): 29–56. https://doi.org/10.1193/1.1585867.
- Stathopoulos, T. 2006. "Pedestrian level winds and outdoor human comfort." *J. Wind Eng. Ind. Aerodyn.* 94 (11): 769–780. https://doi.org/10.1016/j.jweia.2006.06.011.
- Steckley, A., M. Accardo, S. L. Gamble, and P. A. Irwin. 1992. "The use of integrated pressures to determine overall wind-induced response." *J. Wind Eng. Ind. Aerodyn.* 42 (1–3): 1023–1034. https://doi.org/10.1016/0167-6105(92)90108-M.
- Takanashi, K., and M. Nakashima. 1987. "Japanese activities on on-line testing." *J. Eng. Mech.* 113 (7): 1014–1032. https://doi.org/10.1061/(ASCE)0733-9399(1987)113:7(1014).
- Tamura, Y., K. Shimada, and K. Hibi. 1993. "Wind response of a tower (typhoon observation at the Nagasaki Huis Ten Bosch Domtoren)."

- J. Wind Eng. Ind. Aerodyn. 50 (Dec): 309–318. https://doi.org/10.1016/0167-6105(93)90086-4.
- Tschanz, T., and A. G. Davenport. 1983. "The base balance technique for the determination of dynamic wind loads." *J. Wind Eng. Ind. Aerodyn.* 13 (1): 429–439. https://doi.org/10.1016/0167-6105(83)90162-9.
- Xie, J., and P. A. Irwin. 1998. "Application of the force balance technique to a building complex." *J. Wind Eng. Ind. Aerodyn.* 77–78 (Sep): 579–590. https://doi.org/10.1016/S0167-6105(98)00174-3.
- Yang, J. N., A. K. Agrawal, B. Samali, and J. C. Wu. 2004. "Benchmark problem for response control of wind-excited tall buildings." *J. Eng. Mech.* 130 (4): 437–446. https://doi.org/10.1061/(ASCE)0733-9399 (2004)130:4(437).
- Zhou, Y., T. Kijewski, and A. Kareem. 2003. "Aerodynamic loads on tall buildings: Interactive database." *J. Struct. Eng.* 129 (3): 394–404. https://doi.org/10.1061/(ASCE)0733-9445(2003)129:3(394).